

Reynard de Vries¹, Tomas Sinnige¹ & Leo L. M. Veldhuis¹

¹Delft University of Technology, Faculty of Aerospace Engineering, Kluyverweg 1, 2629HS Delft, the Netherlands

Abstract

The goal of this study is to determine the aero-propulsive performance of an over-the-wing distributed propulsion (OTWDP) system, and to understand how it depends on various operating conditions. For this, a wind-tunnel test is performed with a simplified OTWDP geometry consisting of three unducted propellers placed side-by-side above a rectangular wing. A numerical model combining 2D panel methods, a slipstream vortex model, and a lower-order method for propeller performance in non-uniform inflow is then used to analyze additional operating conditions. A comparison to experimental data shows that the numerical method captures the changes in wing and propeller performance due to aerodynamic interaction in cruise conditions, though it is inaccurate if flow separation occurs on the wing surface beneath the propeller. For a setup with propellers of diameter-to-chord ratio 0.6 placed above the wing at 80% chord, the sectional lift-to-drag ratio of the wing is found to increase by 40% - 70% for typical cruise lift and thrust coefficients, while the propeller efficiency is decreased by 10% - 15%, compared to the two components in isolation. Parameter sweeps demonstrate that the combined aero-propulsive performance improves with a variable-pitch propeller and at higher lift coefficients, thrust settings, or Reynolds numbers.

Keywords: over-the-wing propellers, aerodynamic performance, propeller interaction, distributed propulsion, experimental aerodynamics

Nomenclature

Propeller incidence angle [deg] = Speed of sound [m/s], axial induction factor[-] $i_{\rm P}$ a Advance ratio, $V_{\infty}/(nD)$ [-] A'Aspect ratio of rectangular wing, b/c [-] Jl Sectional lift [N/m], length [m] = Span [m] b В = Number of blades [-] L Lift [N] (Freestream) Mach number, V_{∞}/a_{∞} [-] Wing chord [m] Mc Rotational speed [Hz] Sectional drag coefficient, $d/(q_{\infty}c)$ [-] n $C_{\mathcal{A}}$ Normal force [N], number of instances Net system axial force coefficient, N $C_{D,\text{net}}$ $(D+F_{x,P})/(q_{\infty}S_{ref})$ [-] Normal-force coefficient, $N/(q_{\infty}\pi R^2)$ [-] N_c Sectional lift coefficient, $l/(q_{\infty}c)$ [-] c_l Static pressure [Pa], helix pitch [m] p C_{L} Lift coefficient, $L/(q_{\infty}S_{\text{ref}})$ [-] $P_{\rm s}$ Shaft power [W] Net system vertical force $C_{L,\text{net}}$ Dynamic pressure, $0.5\rho V^2$ [Pa] qcoefficient, $(L+F_{z,P})/(q_{\infty}S_{\mathrm{ref}})$ [-] QTorque [N·m] Pressure coefficient, $(p-p_{\infty})/q_{\infty}$ [-] C_p Torque coefficient, $Q/(q_{\infty}\pi R^3)$ [-] $Q_c =$ = Torque coefficient, $Q/(\rho n^2 D_p^5)$ [-] C_Q Radial coordinate [m] r = Thrust coefficient, $T/(\rho n^2 D_{\rm p}^4)$ [-] C_T Radius [m] R = Distance [m], sectional drag [N/m] d Chord-based Reynolds number, $Re_c =$ = Drag [N], diameter [m] D $(\rho V_{\infty} c)/\mu$ [-] $\vec{e}_x, \vec{e}_y, \vec{e}_z$ = Cartesian unitary vectors [-] Reference area [m²] $S_{\text{ref}} =$ = Force [N] Thrust [N] T

 T_c = Thrust coefficient, $T/(q_{\infty}\pi R^2)$ [-] \vec{v} = Cartesian velocity vector [m/s]

 v_r = Radial velocity [m/s] v_θ = Tangential velocity [m/s] V = Velocity magnitude [m/s] W = Weighting function [-] x,y,z = Cartesian coordinates [m]

 α = Angle of attack [deg]

 $\beta_{0.7R}$ = Blade pitch at r/R = 0.7 [deg]

 Γ = Circulation [m²/s]

 $\Delta(\)$ = Change due to interaction

 Δx = Axial spacing [m]

 ε = Error [-]

 ε = Tip clearance w.r.t. wing surface [m] $\eta_{\rm P}$ = Propeller efficiency, $TV_{\infty}/P_{\rm S}$ [-]

 $\eta_{\rm p}$ = Propeller efficiency in flight direction, $-F_{\rm x,P}V_{\infty}/P_{\rm s}$ [-]

 $\eta_{\rm p}(L/D) = \text{Aero-propulsive efficiency [-]}$ $\mu = \text{Dynamic viscosity [Pa·s]}$

 ρ = Air density [kg/m³]

Additional sub- and superscripts

b = Per blade eff = Effective

f = Friction drag component

ind = Induced inst = Installed invisc = Inviscid

iso = Isolated (uninstalled)

max = Maximum

 $\begin{array}{lll} \text{off} & = & \text{Propeller-off conditions} \\ p & = & \text{Pressure drag component} \\ p \rightarrow w & = & \text{Induced by propeller on wing} \\ P & = & \text{Propeller, propeller location} \end{array}$

ps = Pressure side ss = Suction side tr = Transition location

visc = Viscous

 $w \rightarrow p$ = Induced by wing on propeller

1. Introduction

One of the key strategies to reduce the energy consumption of an aircraft is to enhance the efficiency of the propulsion system and its integration with the airframe [1, 2, 3]. For this reason, research efforts into alternative energy sources and powertrain architectures such as (hybrid-)electric propulsion (HEP) have experienced an exponential growth in recent years [4, 5]. A potential advantage of HEP is the ability to spread the propulsive power over multiple, smaller, electrically-driven propulsors without substantially compromising the efficiency or weight of the motors. This is especially interesting for subsonic passenger transport aircraft, where propellers can be placed at strategic locations on the airframe to exploit beneficial aerodynamic interaction effects and enhance the aerodynamic efficiency (L/D) or propulsive efficiency (η_p) of the vehicle. However, substantial overall aero-propulsive efficiency $(\eta_p \cdot L/D)$ benefits must be provided by these "distributed propulsion" systems to overcome the weight penalty typically associated to hybrid-electric powertrains [6].

The over-the-wing (OTW) propeller is a particularly promising configuration in this regard, since it can significantly increase the lift-to-drag ratio of the wing in both cruise [7] and high-lift [8] conditions. For example, the work of Müller et al. [9] suggests a lift-to-drag ratio increase of more than 30%, relative to a tractor configuration. OTW propellers can also enhance the wing high-lift performance if the slipstream is deflected by inclining the propeller [10] or producing a Coandă effect [11], similar to upper-surface blown wings [12]. Additionally, flyover noise may be reduced due to the shielding effects of the wing [13]. But, even though OTW propellers have existed for a century [14], the amount of aircraft featuring such systems is limited. This can largely be attributed to the propeller-efficiency penalty observed in most cases [9, 15], the need for large pylons to support the propeller above the wing, and potentially to a large thrust-induced, nose-down pitching moment. These drawbacks may be compensated if a single large propeller is substituted by multiple smaller ones [16], in an "over-the-wing distributed-propulsion" (OTWDP) arrangement.

However, the actual aero-propulsive performance benefits of OTWDP are currently unclear. Even for a single OTW propeller, some authors have found moderate [8] to drastic [15] reductions in propeller efficiency, while others have found it to increase [7]. Analogously, most studies suggest that the lift increase is maximum for a propeller placed near the trailing edge [15, 17, 16], though in some numerical investigations it has been found to be maximum near the mid-chord [15]. These apparent contradictions suggest that the aero-propulsive efficiency is highly dependent on the design and operating conditions of the system. Such dependencies cannot be explained with conventional (e.g., tractor) propeller-wing interaction studies, since the placement of a propeller above a wing leads to

a fundamentally different interaction problem, as illustrated in Fig. 1. This also makes it difficult to extrapolate the findings of previous studies to distributed-propulsion configurations, where the complexity of the flowfield is further increased due to additional elements such as ducts or adjacent propellers. Although the aerodynamic characteristics of ducted OTWDP configurations have also been investigated on several occasions [18, 19, 20, 21], these geometry-specific analyses provide limited insight into the physical interaction mechanisms that drive the changes in performance.

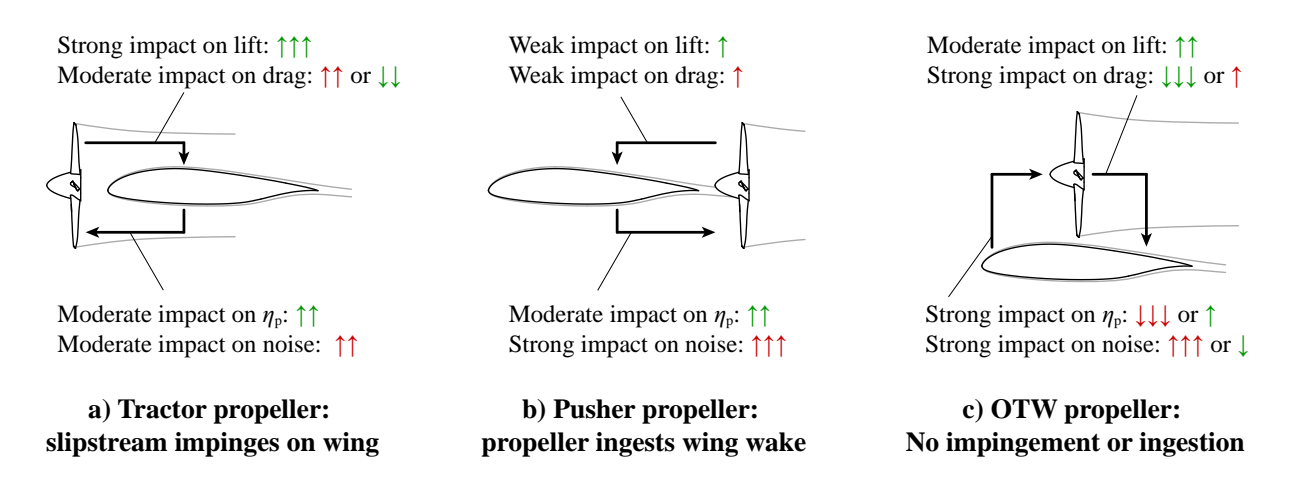


Figure 1 – Typical effects of propeller-wing interaction on the performance of various propeller configurations. Green and red arrows indicate performance benefits and penalties, respectively. For some effects, the impact can be positive or negative depending on the geometry of the system.

The objective of this study is therefore to determine the aero-propulsive performance characteristics of an OTWDP system, to describe the physical mechanisms responsible for the changes in performance, and to assess how they are affected by different operating conditions. Since a priori it is unknown what a "good" duct design would look like, or whether a duct is beneficial from an efficiency perspective in the first place, this study focuses on a series of unducted propellers placed side-by-side above a rectangular wing. The effect of secondary elements such as pylons or nacelles is not addressed. Furthermore, the investigation is limited to cruise conditions, since the high-lift performance is highly sensitive to the specific design and Reynolds number of the system [11]. The use of a highly simplified geometry makes the dominant interaction mechanisms easier to understand, but implies that the performance characteristics differ from a more optimized design. To ensure the results are representative, key non-dimensional parameters such as the lift coefficient, thrust coefficient, or diameter-to-chord ratio are selected to match full-scale applications.

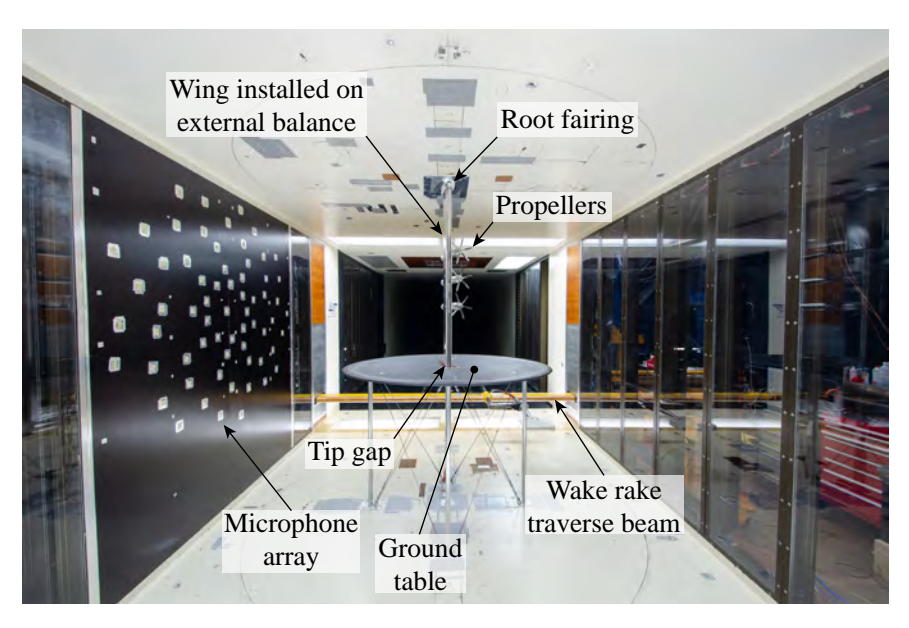
A combined experimental/numerical approach is taken for this investigation. The purpose of the experimental analysis is to provide insight into the aerodynamic performance of a baseline configuration, and to provide a reference data set for the validation of the numerical model. The purpose of the simplified, lower-order numerical model is to assess different operating conditions which are challenging to compare experimentally. Sections 2.and 3.present the experimental and numerical setups, respectively, including a discussion of their limitations. The validation of the numerical model is then performed in Sec. 4.for the baseline configuration analyzed in the experiment. Subsequently, the effect of several operating conditions (thrust setting, lift coefficient, blade pitch, and Reynolds number) is analyzed numerically in Sec. 5.

2. Experimental Setup

2.1 Facility & Model Description

Experiments were performed in the DNW Low-Speed Tunnel (LST), a closed-circuit wind tunnel with a test section of 2.25 m \times 3 m and a maximum freestream velocity of 80 m/s. The purpose of the experiments was two-fold: to analyze the aerodynamic performance of a leading-edge distributed-propulsion (LEDP) configuration in high-lift conditions (not discussed herein), and to analyze the

aerodynamic performance of the OTWDP configuration in cruise conditions. The wing model had a span b of 1.25 m, and was installed vertically on an external balance located on the top side of the test section, as depicted in Fig. 2a. The wing featured the same NLF-MOD22B airfoil [22] used in Ref. [16], including the Fowler flap of 30% chord. Only the flap-retracted position was tested in the OTWDP configuration, since this study focuses on cruise conditions. For these measurements, the flap slot was sealed on the pressure side to prevent the through-flow of air, and transition strips with distributed roughness (carborundum) elements of grit size 60 were placed at 10% and 5% chord on the pressure and suction sides of the airfoil, respectively. The wake-rake and microphone array visible in Fig. 2a were used mainly for the LEDP configuration and are not discussed here.





a) Test section seen from upstream

b) Close-up of model

Figure 2 – Overview of the test section and wind-tunnel model used in the DNW LST campaign.

The diameter-to-chord ratio of the setup was selected as a compromise between the LEDP application, where larger diameter-to-chord ratios are expected (typically $D_{\rm P}/c \sim 1$ or higher; see e.g. Refs. [23, 24]), and the OTWDP configuration, where lower diameter-to-chord ratios are envisioned $(D_{\rm P}/c < 0.5; {\rm see~e.g.~Refs.~[18, 25]})$. This trade-off resulted in a diameter-to-chord ratio of $D_{\rm P}/c = 0.6$ which, for the available propeller geometry, corresponded to a wing chord of c = 0.3 m. Given the modest aspect ratio of the model (A' = 4.16), an end-plate was used to limit the tip effects and minimize the spanwise lift gradient at the location of the propellers. For this, a ground table was positioned beneath the wing model, maintaining a gap of 1.5 mm between the wing and the ground plate to prevent the transmission of forces. The ground table featured an elliptical edge and was produced from a wooden plate of 18 mm thickness and 1.45 m diameter ($D_{\text{table}}/c \approx 5$), as shown in Fig. 3a. Moreover, although a fairing was used in an attempt to reduce junction-flow effects at the wing root (Fig. 2a), tuft visualizations (not shown here) revealed a large wedge of separated flow near the wing root in highlift conditions, due to interaction with the wind-tunnel wall boundary layer. However, for the cruise condition analyzed in the OTW configuration ($C_L < 1.1$, no flap deflection), the *change* in performance due to propeller-wing interaction was considered indicative of what would occur on an infinite wing. This was based on three observations:

- The tufts showed no flow separation or spanwise flow components at the root and tip of the wing for this range of angles-of-attack.
- The two rows of pressure ports (see Sec. 2.2) and wake-rake measurements showed a symmetric behavior around the central part of the wing.
- The clean-wing sectional lift polars obtained from surface-pressure measurements (c_l) were nearly identical to the integral wing lift polars obtained from external balance measurements (C_L) , indicating that a relatively constant spanwise lift distribution was achieved.

Three six-bladed (B=6) propellers of $D_{\rm P}=0.2032$ m were used, such that the changes in wing loading beneath the middle propeller were representative of a distributed-propulsion configuration with many propellers ($N_{\rm P}\gg 1$). Additional information regarding the geometry of these "XPROP-S" propellers can be found in Ref. [26]. The propellers were installed without stagger on the suction side of the wing by means of the same nacelles and support sting as used in Ref. [27]. The support sting was clamped vertically in the ground table and top turntable of the test section, and could be installed at different vertical positions to sample the pressure distribution at various spanwise locations relative to the propellers, using the two rows of pressure taps shown in Fig. 2b. The propellers were installed perpendicularly to the local wing surface at $x_{\rm P}/c=0.8$, corresponding to an incidence angle relative to the wing chordline of $i_{\rm P}=10.2^{\rm o}$ (see Fig. 3b). The tip clearance between the three propellers and between the propellers and wing surface were d=4.4 mm (d/R=0.04) and $\varepsilon=5$ mm ($\varepsilon/c=0.0167$), respectively. Additionally, a small rod, slightly larger than the propeller radius, was attached to each nacelle to act as a safety stop and prevent the wing from touching the propellers in case of an unwanted wing deflection at high angles of attack. A contact sensor attached to the tip of the rods confirmed that there was no contact in the measured angle-of-attack range.

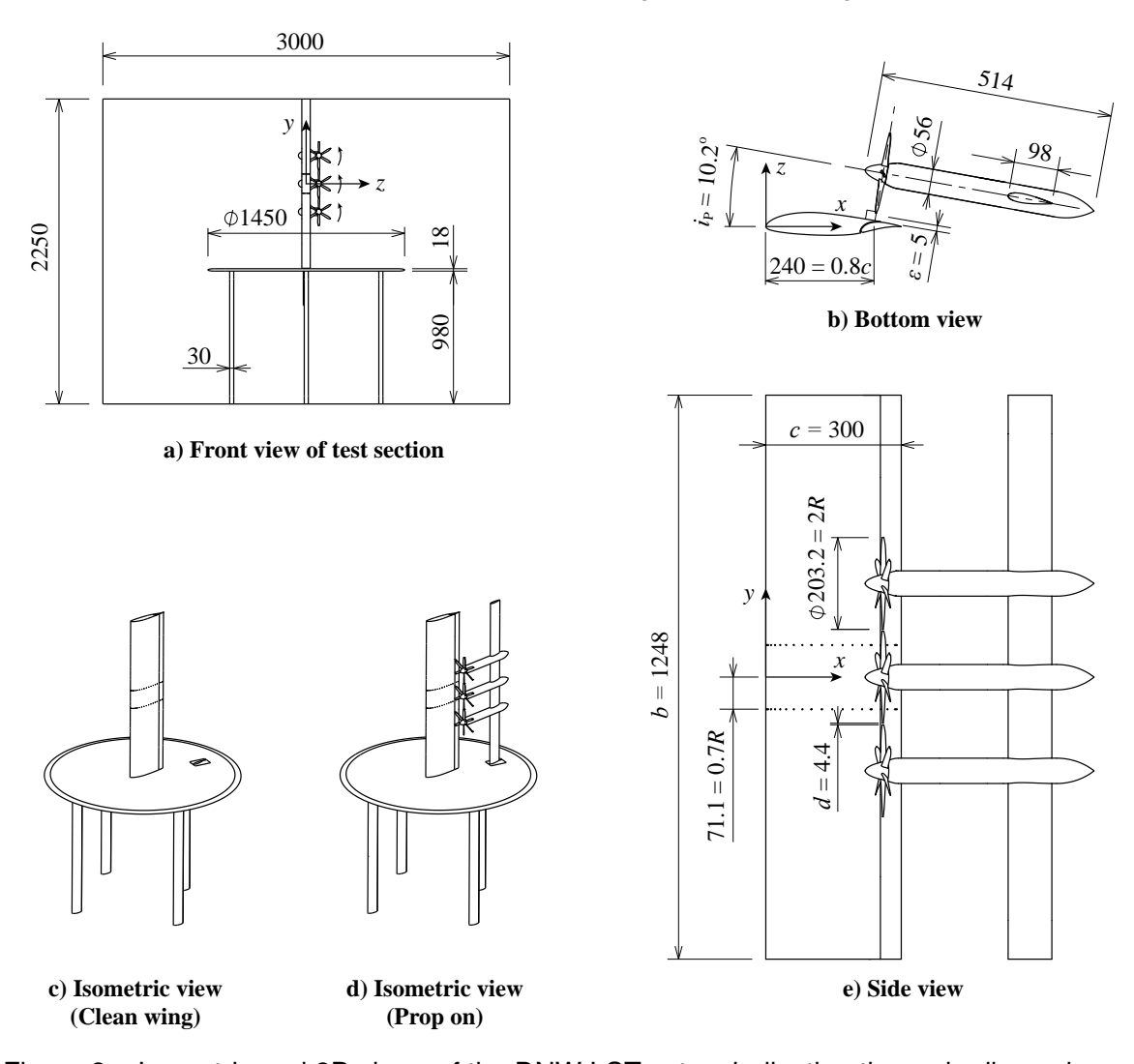


Figure 3 – Isometric and 2D views of the DNW LST setup, indicating the main dimensions, coordinate system ($\alpha=0^{\rm o}$), and rotation direction of the propellers. Safety rods not shown. Dimensions in mm.

2.2 Measurement Techniques

Three types of measurements were performed: external balance measurements, propeller forcesensor measurements, and wing surface-pressure measurements. These measurement techniques

are described in the following subsections. No wind-tunnel wall corrections were applied to the measured data. The wing and ground table occupied approximately 1% and 2% of the cross-sectional area of the test section, respectively, and therefore blockage effects were deemed to be minor. Moreover, the wing chord was small relative to the width of the test section, and only modest lift coefficients were evaluated in the OTWDP setup ($C_L < 1.1$). Therefore, lift interference effects due to the walls were also considered to be small. Consequently, given the complexity of accurately accounting for the effect of the wind-tunnel walls and ground table on the wing performance, it was decided to present the results in their uncorrected form.

2.2.1 External Balance

A six-component external balance was used to quantify the forces on the wing itself. The balance featured a measurement range of 2100 N in the directions of lift and drag, with a 0.1% calibration uncertainty on the full-scale range. Measurements were performed in a "clean wing" configuration (Fig. 3c), with the support sting and propellers ("Prop on", Fig. 3d), and with the support sting without propellers ("Prop off"). In this way, the effect of the support sting and the propellers on the wing loads could be determined separately.

Data were acquired at several angles of attack for each configuration and advance ratio (see Table 1). These angle-of-attack polars were recorded in the same order for each measurement run (i.e., without randomization), with one angle of attack being repeated several times to capture potential deviations throughout a given run due to e.g. hysteresis effects. Additionally, wind-off tare runs were performed to subtract non-aerodynamic forces recorded on the balance when varying the angle of attack, as well as potential calibration offsets. No systematic data fitting was applied to the polars. Instead, the mean of all measurements at a given angle of attack was taken as the "true" value at that angle of attack, and the scatter in data points and the residuals of the wind-off corrections were taken as an indicative measure of the uncertainty. These deviations were found to be small relative to the effect of the propellers on the wing, and small relative to the calibration uncertainty of the balance.

2.2.2 Propeller Internal Force Sensor

An ATI MINI-40E six-component force sensor was used to quantify the forces on the middle propeller. In these dedicated force-sensor measurements, the safety rod behind the middle propeller (see Fig. 2b) was removed to avoid any potential upstream effect on the propeller. The measurement procedure, temperature calibration, data fitting, and uncertainty quantification were performed analogously to the experiments described in Ref. [27]. The isolated-propeller measurements of Ref. [27] were also used as an "uninstalled" reference case. A posterior analysis of the data of the present experiment revealed that the thrust component was not accurately captured, since it was appreciably higher than expected from the isolated-propeller measurements, and on occasions suggested propeller efficiencies greater than unity. The propeller torque and in-plane forces, on the other hand, were found to provide values which were in line with the trends observed in previous studies and data sets. Moreover, these components were accurately reproducible in repeated runs on different days. Since the torque and in-plane forces are predominantly dependent on different strain gauges than the ones used to determine thrust (and in-plane moments), the torque and in-plane force components were considered to provide reliable results, while the thrust component was not used for further analysis.

2.2.3 Wing Pressure Taps

The wing model was instrumented with two rows of pressure taps, located $\pm 0.7R$ from the mid-span location of the wing, as shown in Fig. 3e. Each section contained 45 pressure taps, of which 10 were not used because they were located inside the flap cove. Pressure taps up to 10% and 50% chord on the pressure and suction sides, respectively, were connected to 5 psi (34.5 kPa) pressure sensors, while the remaining pressure taps were connected to 1 psi (6.9 kPa) pressure sensors. The pressure sensors featured a calibration uncertainty of 0.25% of the full-scale range. Pressure data were recorded with the propellers installed at four different vertical positions, thereby sampling the sectional pressure distribution at eight spanwise locations with respect to the middle propeller $(-1.0 < (y-y_P)/R < 1.4)$. The pressure at the trailing edge was estimated by taking the average of the extrapolated pressure values of the upper and lower sides of the airfoil. Therefore, the data point

at x/c=1 is an approximated value, and not a measured value. The deviations observed among repeated measurements were confirmed to be significantly smaller than the effect of the propeller on the wing pressure distribution, and smaller than the calibration uncertainty of the pressure sensors.

2.3 Test Conditions

Table 1 provides an overview of the operating conditions tested in the experiment. All measurements were performed at a freestream velocity of 30 m/s, a blade pitch of $\beta_{0.7R}=30^{\circ}$, with co-rotating propellers, and without controlling the relative phase angle between the propellers. In these conditions, the wing-chord-based Reynolds number is $Re_c\approx 6\cdot 10^5$. Although this value is significantly lower than the Reynolds numbers encountered in full-scale applications, the discrepancy does not alter the nature of the physical interaction mechanisms responsible for the changes in system performance in cruise, which are predominantly inviscid effects—as discussed in Sec. 3. However, the actual values of the *changes* in performance due to aerodynamic interaction at low Re_c are conservative compared to the full-scale case (see Sec. 5.4). For the external balance measurements, angle-of-attack sweeps were performed at three different advance ratios, corresponding to high thrust (J=1.00, $T_c\approx 0.45$), medium thrust (J=1.15, $T_c\approx 0.17$), and near-zero thrust (J=1.35, $T_c\approx 0$), respectively. For the propeller force-sensor measurements, advance-ratio sweeps were performed at $\alpha=2^{\circ}$ and $\alpha=8^{\circ}$.

Table 1 – Overview of test conditions evaluated in the LST experiment.

Parameter	Values
Freestream velocity V_{∞} [m/s]	30
Angle of attack $lpha$ [deg]	$-4 < \alpha < 10$
Blade pitch $\beta_{0.7R}$ [deg]	30
Advance ratio J [-]	0.8 < J < 1.35
Rotation direction	co-rotating

3. Numerical Setup

A numerical method is developed to investigate the effect of additional operating conditions on the performance of the OTWDP system. A simplified, lower-order method is used in order to limit the computational cost, such that the model can be used for future geometry design-space explorations. Several lower-order methods have been developed previously for OTW propellers by authors such as Veldhuis [15], Marcus et al. [16], and Cooper et al. [17]. The comparisons to experimental data performed by these authors showed that these lower-order methods can capture the changes in wing lift and pressure drag with reasonable accuracy, matching the trends observed in experiments, but generally with slight offsets in the lift or drag values. Nonetheless, the level of fidelity is considered appropriate to examine the effect of the main design variables and provide a first performance estimate for conceptual design purposes. Therefore, a similar approach is taken here, though in this case the method is formulated to account for multiple propellers, non-uniform loading on the propellers, and changes in the wing boundary-layer due to the propeller-induced pressure gradients. To limit the conceptual and computational complexity of this numerical method, several simplifying assumptions are made:

- 1. The effect of the propeller on the wing and vice versa are accounted for, but no iterative coupling is included. This assumption is based on the fact that the changes in wing pressure coefficient due to the OTW propeller are significantly lower than the isolated-wing pressure coefficients $(C_p \sim 1$, while $\Delta C_p \sim 0.1$; see Refs. [16, 17]).
- 2. An unswept, high aspect-ratio wing $(A' \to \infty)$ is modeled as a series of independent 2D wing segments. Although each segment accounts for the velocities induced by the propellers in a 3D space, the spanwise velocity component is neglected and the effect of trailing vorticity due to spanwise variations in wing loading is not accounted for. This assumption is based on the experimental results (see Sec. 4.), which show that the changes in lift and drag created beneath the distributed propellers are practically constant in spanwise direction.
- 3. The effect of propeller-propeller interaction is neglected, since Ref. [27] shows that the effect on propeller performance is small.

4. Additional elements such as ducts, nacelles, or pylons are not modeled. Although they may appreciably affect the performance of the system, they require a more detailed geometrical description, a more complex 3D modeling, and make it difficult to break down and understand the physical interaction mechanisms. Hence, only the propeller and wing are investigated.

With these simplifications, the effect of the wing on the propeller and vice versa can conceptually be explained with the 2D representation of Fig. 4. The velocity profile induced by the wing at the propeller location can be decomposed into a change in the effective advance ratio, a change in the effective angle of attack, and a non-uniform-inflow component. Previous research has shown that, for typical OTWDP applications where the propeller is significantly larger than the thickness of the wing boundary layer, the effect of the boundary layer on the propeller performance (component D of Fig. 4a) is negligible [11]. Therefore, the inflow-velocity distribution at the propeller disk can be estimated using, for example, an inviscid 2D panel method. Analogously, the effect of the propeller on the wing can be decomposed into a change in the effective angle of attack, and a non-uniform velocity distribution which is dominant in the vicinity of the propeller disk. These velocities cannot be directly estimated with a blade-element method (BEM) because, unlike for tractor propellers, the velocities induced on the wing by OTW propellers depend on the induced axial and *radial* components *outside* the slipstream, and not on the induced axial and *tangential* components *inside* the slipstream.

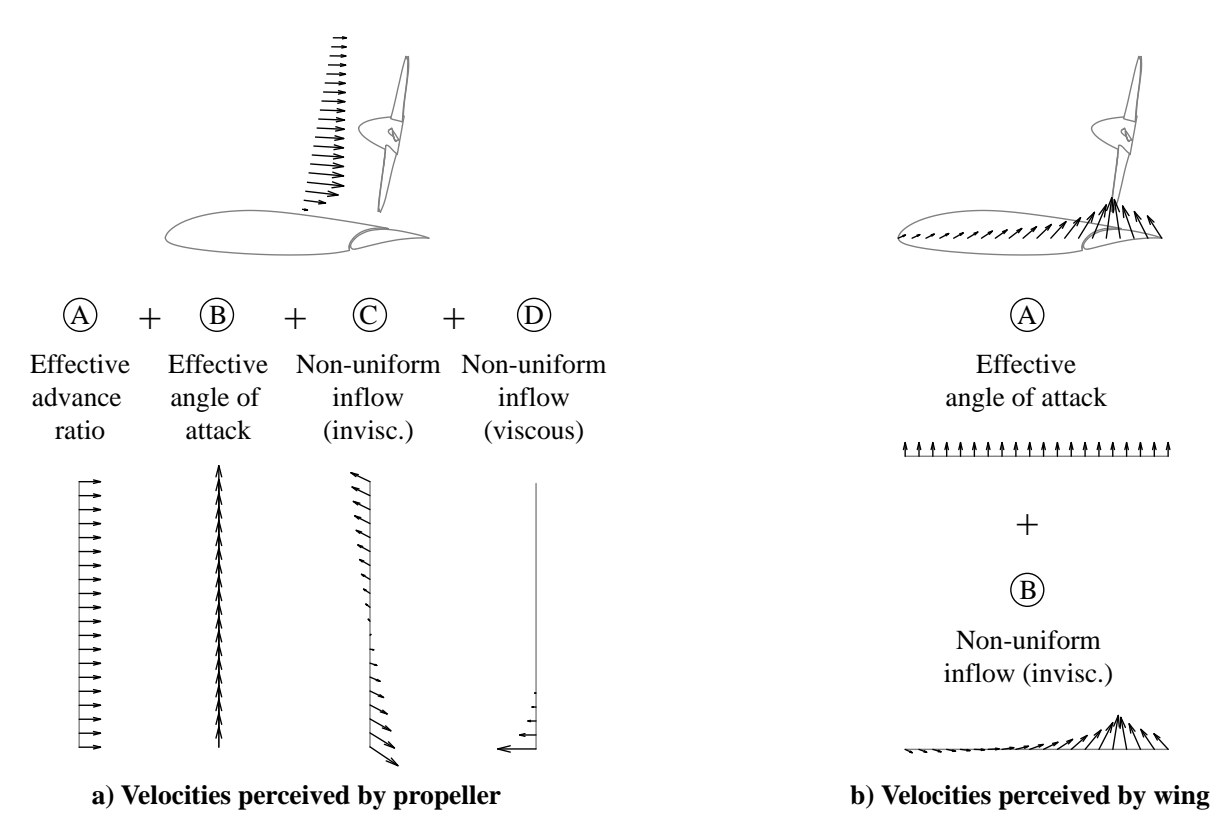


Figure 4 – Conceptual interpretation of the different velocity components contributing to a change in wing and propeller performance from a potential-flow perspective.

To estimate these induced velocities and their subsequent effect on wing and propeller performance, the numerical method models three main components, shown Figure 5a: a propeller-performance model used to estimate the changes in loading on the propeller disk, a slipstream-vortex model used to estimate the velocities induced by the propeller-vortex system, and a series of independent wing sections represented with a 2D panel method. The three modules are described in the following subsections, respectively, and are coupled following the flowchart of Fig. 6. The implementation is performed in Matlab. The computational time required to estimate the performance of an OTW propeller and the wing segment beneath it, including viscous effects, ranges from several seconds to several minutes on a single core, depending on the discretization settings and the initial guess of the inverse airfoil-design process (described in the following sections).

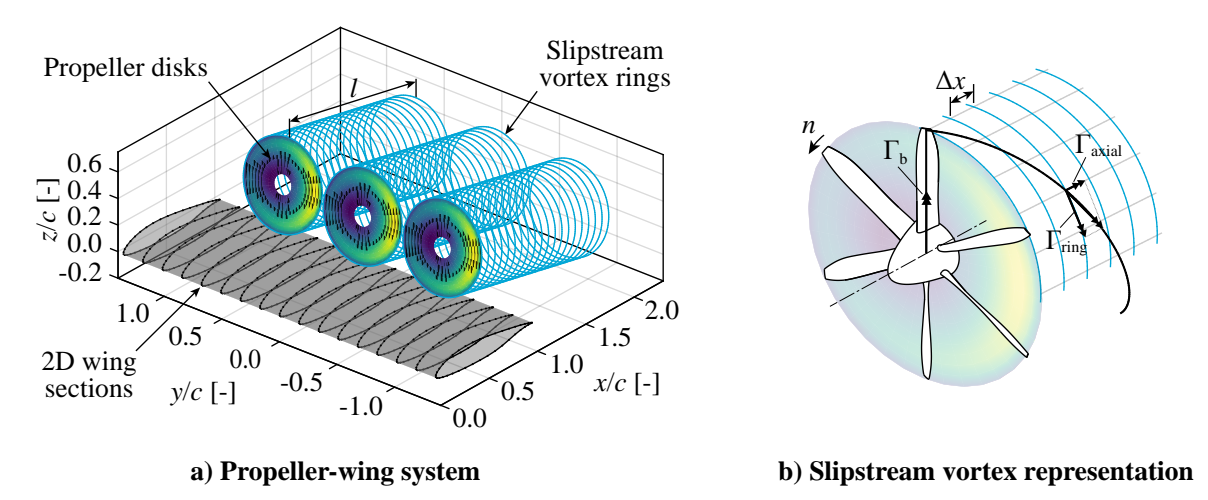


Figure 5 – Overview of the three components modeled in the numerical method: wing section, propeller disk, and slipstream ring vortices (left), including a close-up view of how the slipstream vortices relate to the loading on the propeller disk (right).

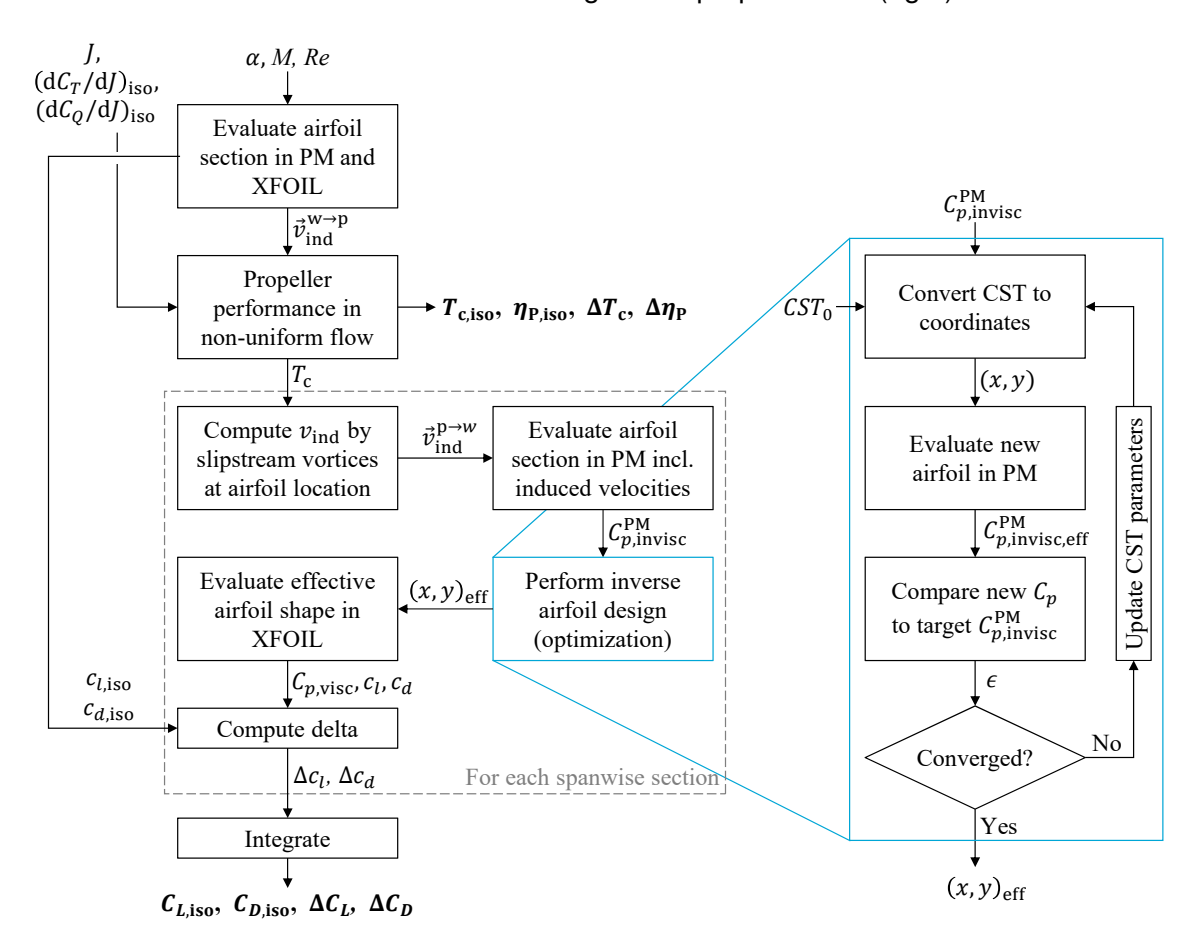


Figure 6 – Top-level flowchart of the numerical method used to estimate cruise performance for a given geometry.

3.1 Propeller Performance Model

The engineering method developed by van Arnhem et al. [26] is used to estimate the performance of the propeller in the non-uniform inflow field generated by the wing. With the aforementioned simplifications, the non-uniform inflow field induced by the wing at the propeller location $\vec{v}_{\text{ind}}^{\text{w}\to\text{p}}$ can be estimated by sampling the velocity induced by the 2D panels representing the wing. This first step is indicated in the top left-hand corner of Fig. 6. The propeller performance model then computes the thrust and torque distribution on the propeller disk for a generic inflow velocity distribution by decom-

posing the local perturbation into axial and azimuthal components. By obtaining the sensitivity of the blade loading to changes in axial and tangential inflow from CFD simulations of the isolated propeller [26], the change in blade loading can be computed for an arbitrary non-uniform inflow field. This change in loading is subsequently integrated over the complete propeller disk to provide the overall propeller forces and efficiency. The sensitivity maps were created for a range of advance ratios for the same geometry and operating conditions as the experimental analysis (XPROP-S, $V_{\infty}=30$ m/s) in earlier work [26].

Although the nacelle is not explicitly modeled in the numerical method, a correction to the in-plane velocity distribution at the propeller disk is included to account for the changes in propeller normal force due to the flow around the nacelle. For this, the cross-flow induced by the nacelle is estimated by taking the in-plane component of the velocity at the center of the propeller disk, $V_P \sin \alpha_P$ (including wing-induced velocities; see Fig. 7), and assuming that it evolves around the nacelle cross-section similarly to the potential flow around a 2D cylinder. In that case, the cylinder can be represented by a doublet and the in-plane velocities induced by the nacelle can be computed analytically as a function of the radius of the nacelle at the propeller location (see e.g. Ref. [28], Ch. 3). Additional analyses performed by van Arnhem [29] confirmed that the in-plane velocities estimated with this simplified approach are comparable to those estimated by RANS simulations of the nacelle at an angle of attack.

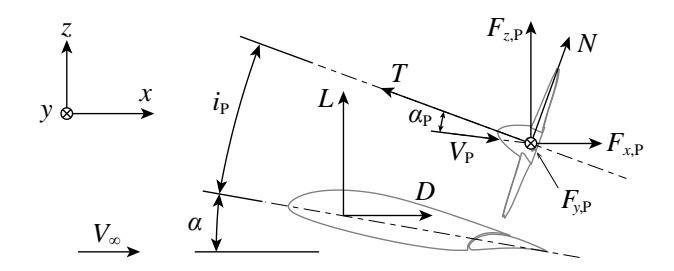


Figure 7 – Definition of force components on the wing and propeller.

Though the selected propeller modeling method provides a rapid estimation of the changes in propeller performance due to the interaction with the wing, it presents some limitations when evaluating the propeller at higher freestream velocities. Most importantly, it is insensitive to changes in the freestream Mach number or Reynolds number, since the sensitivity maps correspond to $V_{\infty}=30$ m/s. Although the method would also be applicable to such conditions if the corresponding isolated-propeller sensitivity maps were computed, this was not performed in the present work. Nevertheless, the effect of Reynolds number on the *changes* in propeller performance are expected to be small, since an increase in Re leads to an offset in the propeller performance curves (see e.g. Ref. [26]), without significantly altering their slope. Hence, the response to a given ΔJ is not significantly affected by the Reynolds number. However, the absolute value of the force and torque coefficients predicted at a given J will be lower than in a full-scale application.

3.2 Slipstream Vortex Model

In a time-averaged sense, the slipstream of a propeller with uniform loading can be represented by a series of axial vorticity lines and tangential vorticity rings [30, 31], as shown in Fig. 5b. It can be shown that, of the various components that constitute the propeller vortex system, only the tangential-vorticity component in the slipstream has an effect on the velocities outside the slipstream, while the axial and radial (i.e., bound) vorticity components only contribute to the velocities inside the slipstream [15]. Therefore, the velocities induced by the propeller on the wing can be estimated by representing the propeller as a series of vortex rings, as shown in Fig. 5a. For simplicity, the propeller slipstream is modeled as a single tube of ring vortices of radius R, neglecting the slipstream deformation due to contraction and the wing-induced velocities. Moreover, the circulation strength is related to the average thrust on the propeller disk. In other words, the circulation. Although this is inconsistent with the non-uniform loading computed in the previous section, a more refined representation of the

slipstream including radial and circumferential discretizations of different strengths was found to have no significant influence on the wing pressure distribution.

The bound vortex strength of a single blade Γ_b can be approximated by applying the Kutta–Joukowski theorem at the mid-span of the blade, assuming that the blade drag is small compared to the blade lift, and that the induced swirl in the propeller plane is small compared to the rotational speed of the blade. In that case, it can be shown (see e.g. Ref. [32]) that

$$\Gamma_{\rm b} pprox rac{T/B}{
ho \pi n R^2},$$
 (1)

from which it follows that the total circulation of all bound (and therefore, tip) vortices can be expressed as a function of the thrust coefficient as

$$\Gamma \approx \frac{T_{\rm c}V_{\infty}^2}{2n}.\tag{2}$$

The circulation strength of each ring vortex can then be calculated by considering the total amount of tangential circulation contained in the helical tip vortices between two subsequent vortex rings separated by a distance Δx , leading to

$$\Gamma_{\rm ring} = \frac{\Delta x}{p} \Gamma,$$
 (3)

where the helix pitch p can be estimated based on the axial induction at the propeller disk a from

$$p = \frac{(1+a)V_{\infty}}{n},\tag{4}$$

$$a = \frac{1}{2} \left(\sqrt{1 + T_{\rm c}} - 1 \right). \tag{5}$$

In Eq. 4 it is assumed that the tip vortices translate in axial direction at a constant velocity $V_{\infty}(1+a)$. This simplified approach therefore again neglects any downstream acceleration or contraction of the slipstream. The assumption of no contraction is considered valid for cruise conditions, in which case only low thrust coefficients are attained and the contraction is negligible. The velocities induced by each vortex ring $[v_r, v_{\theta}] = f(\Gamma_{\text{ring}}, R, x, r)$ are subsequently computed using the analytical expression derived by Yoon and Heister [33]. Finally, the contributions of all rings are summed to obtain the velocity induced by a single slipstream. This process is repeated for each of the N_P propellers to give the total induced velocity at a determined location on the wing.

Figure 8a shows an example of the velocity field induced in the y/R=0 plane by a propeller at a low thrust setting. The figure shows the location of the wing for reference, although the velocities induced by the wing are not included. The velocity increase across the propeller disk is clearly visible. Moreover, the slipstream appears as a straight tube, since contraction is neglected and the gradual alignment of the slipstream center-line with the freestream velocity is not accounted for. Figure 8b presents the corresponding out-of-plane component of the curl of the velocity field. It shows that the magnitude is non-zero in the vicinity of the slipstream edge, particularly at the propeller location. Therefore, the flow is not irrotational everywhere in the domain. This effect grows with increasing thrust setting and has an effect on the solution of the panel method, as discussed in the following section.

3.3 Wing Model: 2D Panel Methods

Two panel methods are used in the numerical model: a 2D panel method implemented directly in Matlab, and XFOIL [34]. The purpose of former (hereafter referred to as "PM" to distinguish it from XFOIL) is to compute the velocities induced by the (inviscid) wing at the propeller location, and to solve the (inviscid) pressure distribution on the wing when subjected to the propeller-induced velocities. It models the panels as linear-strength vortex distributions, following the procedure presented by Katz and Plotkin [28], and accounts for compressibility effects using the Karman-Tsien correction (see e.g. Ref. [35], Ch. 11). The propeller-induced velocities are added to the right-hand-side of the

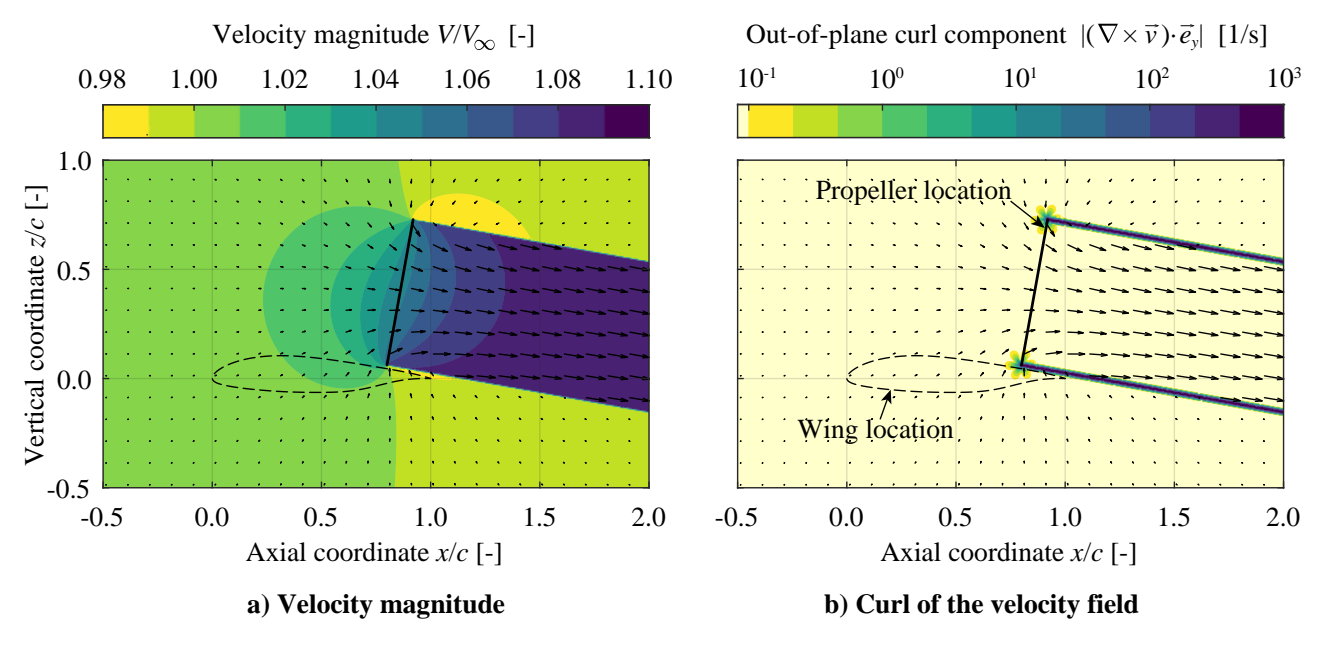


Figure 8 – Example of the velocity magnitude (left) and curl of the velocity field (right) created by the propeller (including V_{∞} ; excluding wing-induced velocities) at a low thrust setting. Velocity vectors indicate the in-plane induced velocities (i.e., excluding V_{∞}).

linear set of equations. In this way, the panel vortex strengths are such that they induce a normal velocity at each panel collocation point which is equal in magnitude but opposite in sign the normal component of the freestream velocity *plus* the propeller-induced velocity.

The purpose of XFOIL, on the other hand, is to account for viscous effects. It must be combined with the PM because, on its own, it cannot account for the propeller-induced effects. The two panel methods were confirmed to produce the same results for an isolated airfoil in inviscid flow. While the friction drag was found to not be significantly affected by the propeller, the change in boundary-layer thickness due to the propeller-induced pressure gradients was found to play a significant role in the lift and pressure drag. Therefore, neglecting the viscous effects would lead to an over-estimation of the lift enhancement and drag reduction.

The way in which these two methods are combined is shown in Fig. 6. XFOIL is first run for a determined set of operating conditions (α, M, Re_c) to provide the lift and drag of the isolated 2D wing. Boundary-layer transition is enforced at the location of the trip strips in the experiment, i.e. at 5% and 10% chord on the suction and pressure sides, respectively. The PM is then used to compute the velocities induced by the wing at the propeller location. This step does not account for changes in the wing-induced velocities at the propeller location due to viscous or compressibility effects. After computing the propeller performance, the velocities induced by the slipstream ring vortices at the panel collocation points of a given spanwise wing section $\vec{v}_{\rm ind}^{\rm p\to w}$ are computed. The PM is subsequently solved including these velocities, thereby providing the inviscid pressure distribution on the wing section including propeller effects, $C_{p,\rm invisc}^{\rm PM}$. To account for viscous effects, the boundary layer has to be solved for this pressure distribution. For this, an equivalent or "effective" airfoil shape $(x,y)_{\rm eff}$ has to be determined which produces the same pressure distribution in uniform inflow as the original airfoil shape in non-uniform flow.

3.3.1 Inverse Airfoil Design Procedure: Optimization

To account for the change in the wing boundary layer due to the propeller-induced velocities, the effective airfoil shape corresponding to a predetermined pressure distribution has to be found. For a wide range of representative pressure distributions this can be done explicitly, and XFOIL includes this functionality. However, the inverse-design routine of XFOIL was found to produce unreliable results in this study, due to the sensitivity to noise in the curvature distribution of the airfoil, and because each time the input pressure distribution is modified slightly in XFOIL to satisfy the Lighthill constraints [36]. This suggests that, in fact, there is no mathematical solution which satisfies the

Lighthill constraints [37] and exactly replicates a generic propeller-on pressure distribution. Hence, an optimization approach is taken instead to find an airfoil shape whose pressure distribution resembles the propeller-on pressure distribution as closely as possible. Although this significantly increases the computational time of the method, it provides more reproducible results.

The steps of this inverse airfoil design optimization are shown on the right-hand-side of Fig. 6. For the optimization, the airfoil shape is parametrized using the class-function/shape-function transformation (CST) described by Kulfan [38]. In this parametrization, the upper and lower sides of the airfoil are represented by a series of Bernstein polynomials multiplied by scaling coefficients, referred to here as "CST coefficients". To reduce the number of design variables, and based on the conceptual breakdown of Fig. 4, it was hypothesized that the effect of the propellers on the wing pressure distribution could be replicated by changing the angle of attack of the airfoil, and modifying the curvature on only the suction side of the airfoil. Hence, the CST design variables are limited to the upper side. Moreover, to ensure a smooth leading edge, the first CST coefficient of the suction side is also kept constant. This does not suppose a major limitation to the design space, as long as the propeller is not placed close to the leading edge. Analogously, the lower bound of the last CST coefficient on the suction side is set to the value of the last CST coefficient on the pressure side, to avoid self-intersecting geometries. Therefore, for an airfoil parametrized with $N_{\rm CST}$ coefficients per side, the number of design variables in the optimization problem is N_{CST}: one design variable for the effective angle of attack, and $N_{\rm CST}-1$ design variables describing the upper surface of the airfoil. The initial guess for the design variables, CST_0 , are the CST coefficients of the original airfoil shape. No additional constraints are imposed, and a gradient-based optimization is performed to find the airfoil shape which minimizes the difference between the airfoil's pressure distribution $C_{p,\mathrm{invisc,eff},i}^{\mathrm{PM}}$ and the target propeller-on pressure distribution of the original airfoil, $C_{p,\text{invisc}}^{\text{PM}}$. For this, the new airfoil created in each iteration is solved in the PM and the resulting error (objective function) is computed as

$$\varepsilon = \frac{\sum_{i=1}^{N_{\text{panels}}} \left| C_{p,\text{invisc},i}^{\text{PM}} - C_{p,\text{invisc},\text{eff},i}^{\text{PM}} \right| \cdot W_i}{\sum_{i=1}^{N_{\text{panels}}} W_i},$$
(6)

where the summation operates over each of the N_{panels} panels of the discretized airfoil, and $W = 1 + k_1 \exp(-k_2 \cdot x/c)$ is a generic weighting function ($k_1 = 2$, $k_2 = 40$) that associates more weight to points near the leading edge in order to capture the suction peak and stagnation point more accurately.

An example of an inverse-design result is given in Fig. 9. The pressure distributions given by dashed and solid black lines correspond to the inviscid wing-pressure distribution without and with propeller-induced velocities, respectively. The wing shape is shown in black in Fig. 9b. The optimization results in the airfoil shape shown in blue, which presents an increase in camber on the suction side, mainly upstream of the propeller location. If this airfoil is solved at the effective angle of attack $\alpha_{\rm eff}$ obtained from the optimization, the pressure distribution shown in blue in Fig. 9a is obtained. The pressure distribution closely resembles the propeller-on pressure distribution, confirming the earlier hypothesis that the effect of the propeller on the wing can be modeled as an increase in the effective angle of attack and a change in the upper-surface curvature. However, some difference between the actual prop-on pressure distribution and the effective airfoil's pressure distribution can be observed, particularly at the suction peak or on the pressure side for x/c < 0.4.

3.3.2 Calculation of Wing Lift and Drag

The sectional lift c_l and pressure drag c_{dp} of each wing section are estimated by integrating the pressure distribution given by

$$C_p = C_{p,iso} + \Delta C_p. \tag{7}$$

However, Fig. 9 shows how the effective airfoil gives only an approximation of the actual pressure distribution. Hence, the change in pressure, ΔC_p , is obtained from

$$\Delta C_{p} = \Delta C_{p,\text{invisc}}^{\text{PM}} + \left(\Delta C_{p,\text{visc}}^{\text{XFOIL}} - \Delta C_{p,\text{invisc}}^{\text{XFOIL}}\right),\tag{8}$$

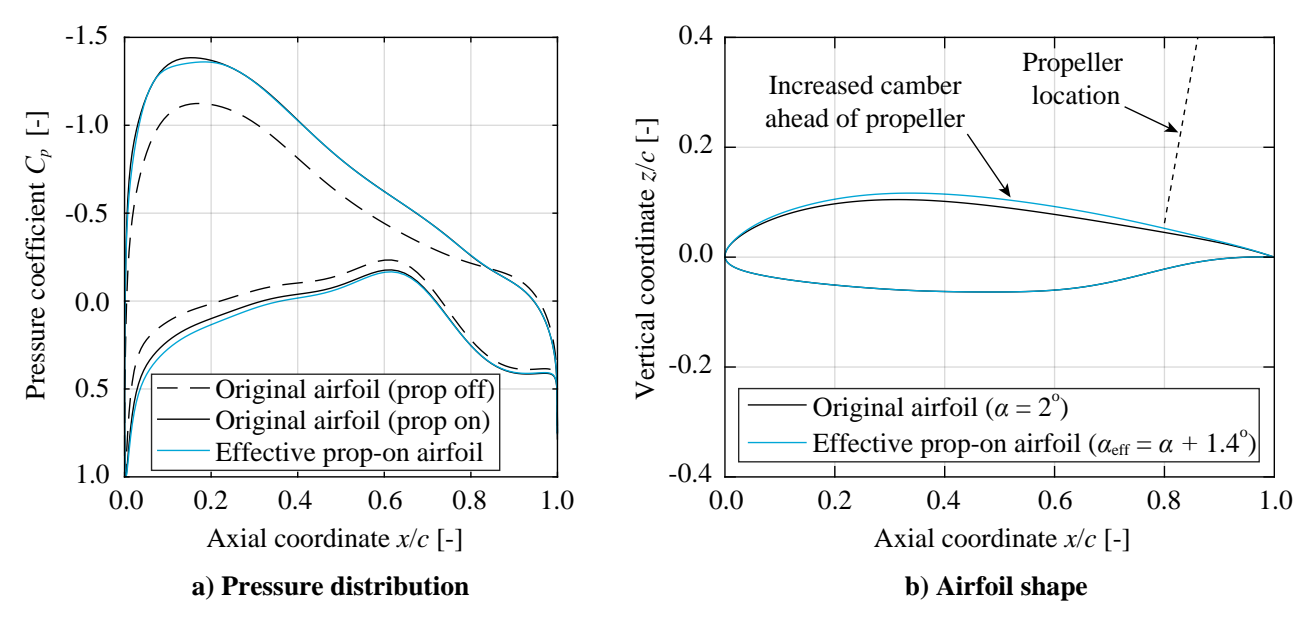


Figure 9 – Inverse airfoil design example (J = 1.00), comparing the pressure distributions obtained by the PM for the effective airfoil shape, and the original airfoil with propeller-induced velocities.

with

$$\Delta C_{p,\text{invisc}}^{\text{PM}} = C_{p,\text{invisc}}^{\text{PM}} - C_{p,\text{invisc,iso}}^{\text{PM}}, \tag{9}$$

$$\Delta C_{p,\text{visc}}^{\text{XFOIL}} = C_{p,\text{visc,eff}}^{\text{XFOIL}} - C_{p,\text{visc,iso}}^{\text{XFOIL}}, \tag{10}$$

$$\Delta C_{p,\text{invisc}}^{\text{XFOIL}} = C_{p,\text{invisc,eff}}^{\text{XFOIL}} - C_{p,\text{invisc,iso}}^{\text{XFOIL}}.$$
(11)

Equation 8 shows that the ΔC_p obtained from the PM is corrected by the term in parenthesis, which is the ΔC_p due to the change in boundary-layer behavior between the propeller-on and propeller-off cases. Note that $\Delta C_{p,\mathrm{visc}}^{\mathrm{XFOIL}}$ is not equal to ΔC_p , since the "propeller on" pressure distribution evaluated in XFOIL is only an approximation of the actual propeller-on pressure distribution and therefore $\Delta C_{p,\mathrm{invisc}}^{\mathrm{PM}} \neq \Delta C_{p,\mathrm{invisc}}^{\mathrm{XFOIL}}$. The friction drag component $c_{d\mathrm{f}}$, on the other hand, is obtained directly from XFOIL.

The 3D aerodynamic force coefficients can be obtained by performing the previous steps for different spanwise locations along the wing. Assuming that the OTWDP system contains many propellers, the lift and drag coefficients of the wing segment associated to one propeller located at y/R=0 can be calculated from

$$C_L = \frac{1}{2R+d} \int_{-R-d/2}^{R+d/2} c_l dy,$$
 (12)

$$C_D = \frac{1}{2R+d} \int_{-R-d/2}^{R+d/2} (c_{dp} + c_{df}) dy.$$
 (13)

An initial investigation of the spanwise lift and drag distributions, however, showed inconsistent local peaks at spanwise locations close to the propeller axis. This effect was more pronounced for higher thrust settings and smaller tip clearances. At these locations, the propeller-on C_p distribution obtained from the PM was found to present a sharp spike at the trailing edge. A closer inspection of the PM with more elementary disturbances revealed that the pressure distribution was smooth if subjected to an infinite 2D vortex (which produces an irrotational velocity field everywhere except at the vortex location), while presenting the trailing-edge spike if subjected to a finite 2D vortex segment (which does not produce an irrotational velocity field¹). Based on this analysis it was concluded that these

¹The tangential velocity induced by a finite vortex filament of length dl scales with $1/r^2$, while the tangential velocity induced by an infinite 2D vortex scales with 1/r. The curl of the velocity field generated by the latter is zero, while the curl of the former is not.

spikes were an artifact of the rotational flow field, which violates the underlying assumption of potential flow models. As seen in Fig. 8b, the curl of the velocity field produced by vortex rings is non-zero, particularly near the slipstream edge. Therefore, although a mathematical solution for the singularity strengths on the airfoil panels exists, the physical meaning of this solution is inaccurate if the panels are close to the slipstream edge.

To minimize the impact of this limitation of the selected numerical approach, two modifications were made to the loading distributions. First, the estimated lift and drag values of airfoil sections with a chordline located at a distance of less than 1.2R from the center of the propeller disk were removed and replaced by interpolating the lift and drag coefficients of the adjacent wing sections. Interpolation was considered an acceptable approach because the experimental data showed that the lift and drag present smooth distributions (see Sec. 4, Fig. 12), and therefore the sectional lift and drag values estimated beneath the edges of the propeller disk are also representative of the values beneath the propeller axis. With the selected "cut-off radius" of 1.2R, this meant that a significant portion ($\sim 50\%$) of the wing span covered by each propeller was interpolated. This highly conservative value was selected such that the same 1.2R margin could be applied for all thrust settings, as well as for additional propeller positions and tip clearances which are not discussed in this article. And second, the ΔC_p values downstream of x/c=0.95 were extrapolated and the trailing-edge pressure was calculated as the average of the pressure and suction sides, similar to the experimental data. These two approximations further highlight the need for a dedicated validation study, discussed in Sec. 4.

3.4 Verification: Convergence Study

A convergence study was performed to estimate the discretization error and verify that the numerical method was correctly implemented. The numerical method contains three modules which are sensitive to discretization error: the slipstream vortex model and the two panel methods (PM and XFOIL). For the slipstream vortex model, different slipstream tube lengths and vortex ring spacings were evaluated. For the panel methods, different numbers of panels and CST coefficients were compared. Only the key findings are summarized here for brevity; additional information can be found in Ref. [39]. Regarding the slipstream vortex model, a slipstream tube of 500 rings with a total length of l=5c was selected. For the panel methods, 200 panels were selected to represent the airfoil. Moreover, 12 CST coefficients were selected to parametrize the suction side of the airfoil in the inverse-design process. Although no systematic uncertainty quantification was performed, the trends suggest discretization errors of the order of $\Delta c_l \sim 0.01$ and $\Delta c_{dp} \sim 0.0005$ for the propeller-induced changes in sectional lift and pressure drag, respectively.

4. Baseline Experimental Results & Numerical Validation

This section presents the results of the experimental campaign to provide a basic understanding of how the propeller and wing affect each other's performance. The results are simultaneously compared to the predictions of the numerical model, to assess to what extent it is capable of capturing the physical trends. The results are divided into two subsections, which focus on the impact on propeller performance and on wing performance, respectively.

4.1 Propeller Performance

Figures 10 presents the thrust, torque, and normal-force coefficients of the middle propeller obtained from the numerical and experimental setups. Isolated-propeller thrust and torque, obtained from Ref. [27], are included in for reference. Since the isolated propeller is evaluated at $\alpha=0^{\circ}$, the corresponding in-plane forces are zero. The numerical results of Fig. 10a indicate that, in the OTW configuration, the propeller thrust is reduced over the full range of advance ratios. This is in line with the findings of previous experimental analyses [39], although the thrust component could not be quantified in the present experiment (see Sec. 2.2). A comparison of the experimental and numerical isolated-propeller thrust curves, however, shows a difference in slope between the two methods. This is predominantly due to a difference in the CFD simulations used to produce the propeller sensitivity maps, which are less sensitive to variations in the blade Reynolds number—as detailed in the validation studies of Ref. [26]. A similar effect is observed in the torque curves of Fig. 10b. In this case, a

comparison of the isolated and installed configurations shows that the numerical model captures the amplitude of the torque reduction accurately at low advance ratios, while it over-predicts the torque reduction at high advance ratios. While the effect of this over-prediction on the change in propeller efficiency $\Delta\eta_P$ cannot be compared due to the lack of thrust data in the experiment, additional analyses performed by van Arnhem et al. in the validation studies of Ref. [26] suggest that the error in the predicted propeller efficiency is of the order of $\Delta\eta_P \pm 0.01$, for an inflow comparable to the one encountered here.

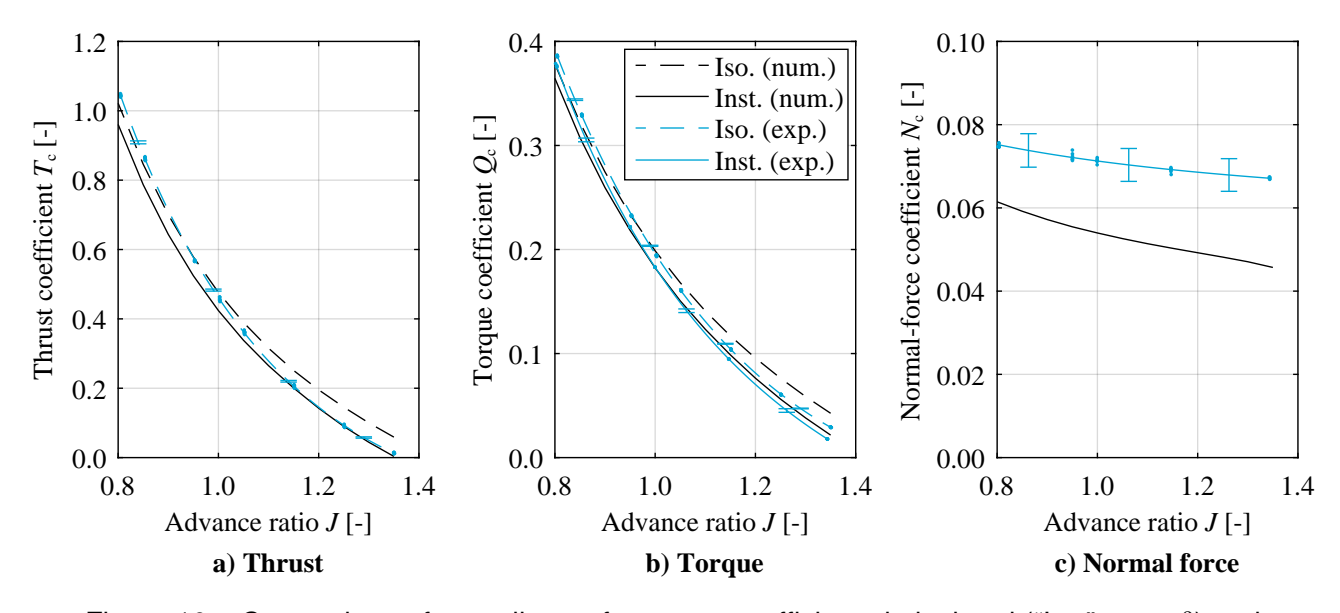


Figure 10 – Comparison of propeller performance coefficients in isolated ("Iso.", $\alpha = 0^{\circ}$) and installed ("Inst.", $\alpha = 2^{\circ}$, $i_P = 10.2^{\circ}$) configurations. Markers indicate individual measurements.

Moreover, Fig. 10c shows that the normal force decreases with advance ratio, attaining a non-zero value at zero thrust ($J \approx 1.35$), due to the in-plane velocities induced by the wing and nacelles. The numerical model under-estimates the normal force on the propeller, as expected from Ref. [26]. However, the normal-force discrepancy is slightly larger in this case, being under-predicted by 20% to 30% at high and low thrust settings, respectively. This can be attributed to the forces on the spinner (which are not included in the numerical model), an incorrect modeling of the nacelle, or to an under-prediction of the wing-induced flow angle at the propeller location α_P . For this configuration, an under-estimation of the normal force contributes to conservative results regarding the overall system performance, since the net vertical force of the propeller-wing system would in reality be higher than estimated.

4.2 Wing Performance

4.2.1 Sectional Pressure Distributions

The effect of the propeller on the wing pressure distribution is shown for two operating conditions in Fig. 11. The experimental C_p distributions presented in Fig. 11a and 11d correspond to the port row of pressure taps (y/R=-0.7) when the vertical position of the support sting is centered around the mid-span of the wing, as depicted in Fig. 3. The effect of the propeller is examined by comparing the propeller-on to the propeller-off measurements (instead of the clean wing), which both include the effect of the nacelles and support sting. The effect of the support sting and nacelles on the wing loads is addressed in subsequent figures. Note that, in the numerical model, the "propeller-off" and "clean wing" configurations are identical, since the nacelles and support sting are not modeled. Figure 11a shows that, for a low lift and thrust setting $(c_{l,\text{off}}=0.38, T_c\approx 0.17)$, the propeller reduces the suction-side pressure upstream of the propeller location $(x_P/c=0.8)$ and increases it downstream of it—as observed in earlier studies [17, 15, 16]. The pressure distributions obtained from the numerical model (Fig. 11b) are qualitatively similar, although a slightly higher suction peak is observed. This

difference is primarily attributed to tip and root effects on the wing in the experiment, which decrease the lift along the entire wingspan. Nevertheless, Fig. 11c shows that the numerical method can

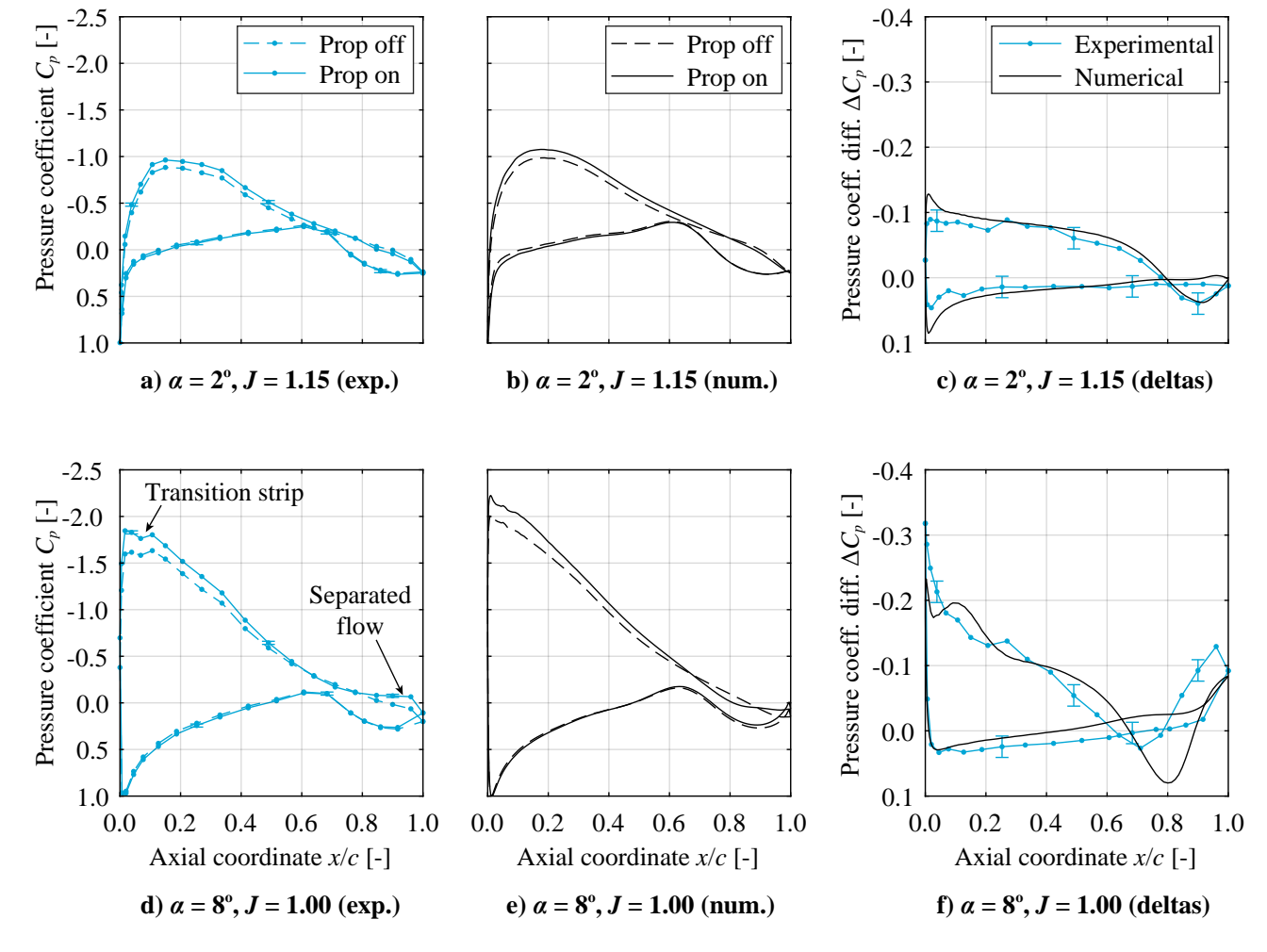


Figure 11 – Wing pressure distributions at y/R = -0.7, obtained from the numerical and experimental setups for low lift, low thrust (top) and high lift, high thrust (bottom) settings.

capture the *changes* in the C_p distribution with reasonable accuracy for these conditions, deviating from the experimental data by up to $\Delta C_p \pm 0.04$ near the leading edge.

The upstream suction generated by the propellers is also visible at higher angles of attack and thrust settings, as shown in Fig. 11d. Downstream of the propellers, the behavior is different than in Fig. 11a. The combination of a strong adverse pressure gradient on the airfoil and a strong adverse pressure gradient beneath the propeller disk leads to flow separation at the axial location of the propeller, as observed in Ref. [11]. However, for these operating conditions, the numerical model predicts a more downstream flow separation then the one recorded in the experiment (Fig. 11e). This leads to a higher pressure near the propeller location (x/c = 0.8), which is especially evident in the ΔC_p distribution of Fig. 11f. As expected from earlier studies [11, 40], the flow separation triggered by the propeller-induced pressure gradients cannot be captured accurately with simplified analyses like a 2D panel method.

4.2.2 Spanwise Loading Distributions

The spanwise loading distributions are shown in Fig. 12 for the same conditions as the pressure distribution of Figs. 11a–11c. In Fig. 12, the horizontal axis is expressed relative to the spanwise location of the center of the middle propeller. The experimental data of Fig. 12a shows that the lift is practically constant in the spanwise interval evaluated, in both the propeller-on and propeller-off conditions. Furthermore, the difference between the propeller-on and propeller-off measurements, Δc_l , is also practically constant in spanwise direction. This is different than for a single OTW propeller, where the propeller creates a bell-shaped Δc_l distribution [7, 10, 9]. In the distributed-propeller configuration, for the chosen propeller separation distance d, the superposition of these bell-shaped loading distributions created by each propeller leads to an approximately constant change in lift.

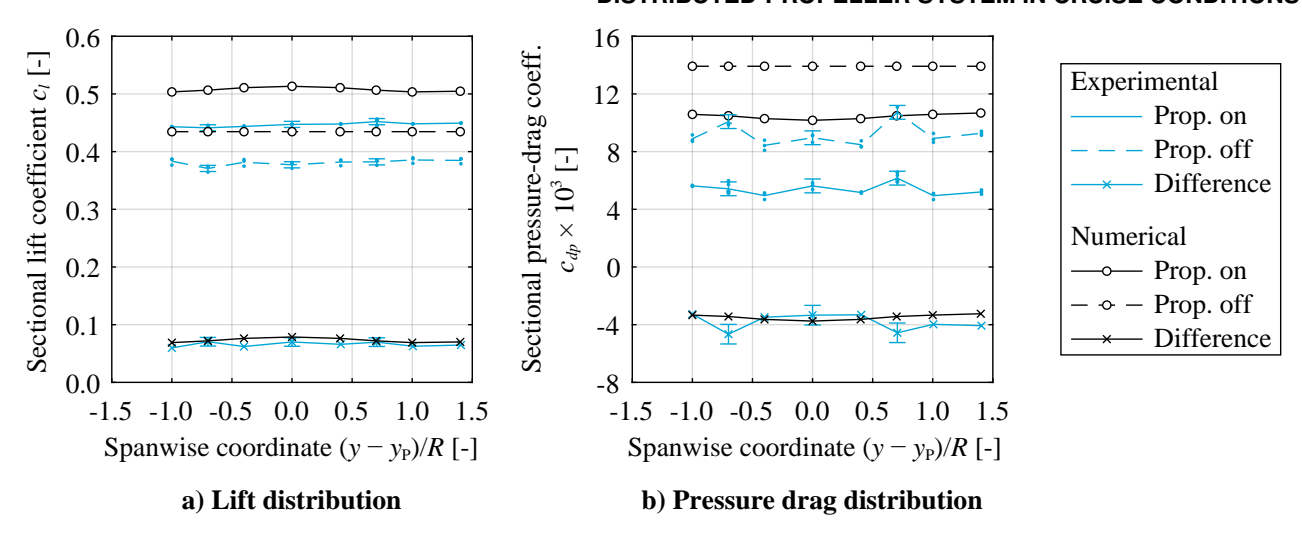


Figure 12 – Spanwise loading distributions along the wing in the three-propeller configuration, for $\alpha = 2^{\circ}$, J = 1.15; blue dots indicate individual measurements.

The spanwise drag distribution, provided in Fig. 12b, presents more distinguishable spanwise variations in the experimental results. The propeller provides a significant reduction in pressure drag; in this condition, the propeller-on pressure drag is approximately half of the value corresponding to the propeller-off case. When moving from $(y-y_P)/R = \pm 1$ towards the propeller axis $((y-y_P)/R = 0)$, the drag reduction due to the propeller Δc_{dp} first increases (in magnitude), as the pressure rise generated on the aft part of the airfoil (see Fig. 11a) increases. However, close to the propeller axis, the drag reduction drops again. This occurs because the strong adverse pressure gradient beneath the propeller causes the boundary layer to thicken, reducing the effective camber near the trailing edge. The relatively constant Δc_l and Δc_{dp} values in spanwise direction justify the quasi-2D approach used to model the wing sections in the numerical method. Fig. 12 shows that the method over-predicts the sectional lift and drag in both the propeller-on and propeller-off cases, as expected from the pressure distributions of Fig. 11. However, the change in lift due to the propeller matches the experimental data well for this operating condition. On average, the change in drag is also captured with reasonable accuracy, although the numerical method does not capture the local reductions observed in the experimental data at $(y-y_P)/R = \pm 0.7$. Nevertheless, these results confirm that, despite the interpolation procedure described in Sec. 3.3.2, the method is capable of predicting the change in wing loading in these conditions.

4.2.3 Lift and Drag Polars

To analyze how the lift and drag of the wing vary with angle of attack and thrust setting, Fig. 13 presents the sectional lift and pressure-drag polars obtained at the same spanwise location as the C_p distributions of Fig. 11. The lift polars of Fig. 13a show that the support sting and nacelles have a negligible effect on the sectional lift at this location. In the propeller-on cases, the lift polars present an offset with respect to the propeller-off cases, similarly to earlier research [20]. This reinforces the interpretation of Fig. 4b, where the increase in wing lift is associated to an increase in the effective angle of attack. In this sense, OTW propellers are very different from tractor propellers, where the lift-curve slope of the wing is increased due to the higher dynamic pressure in the slipstream [15]. The lift polars obtained from the numerical model (Fig. 13b) show a similar offset to the ones of the experiment (Fig. 13a), although in this case the offset reduces more prominently at higher angles of attack.

Figure 13d shows that the support sting and nacelles have a significant effect on the wing pressure drag, particularly for high angles of attack. When comparing the propeller-on and propeller-off cases, an appreciable drag reduction is observed, especially at low angles of attack. The occurs for two reasons. On one hand, the propeller induces an effective angle of attack (effect A in Fig. 4b), thus tilting the lift-vector forward and leading to a negative drag contribution. This leads to a drag reduction for any axial position of the OTW propeller. On the other hand, outside the slipstream,

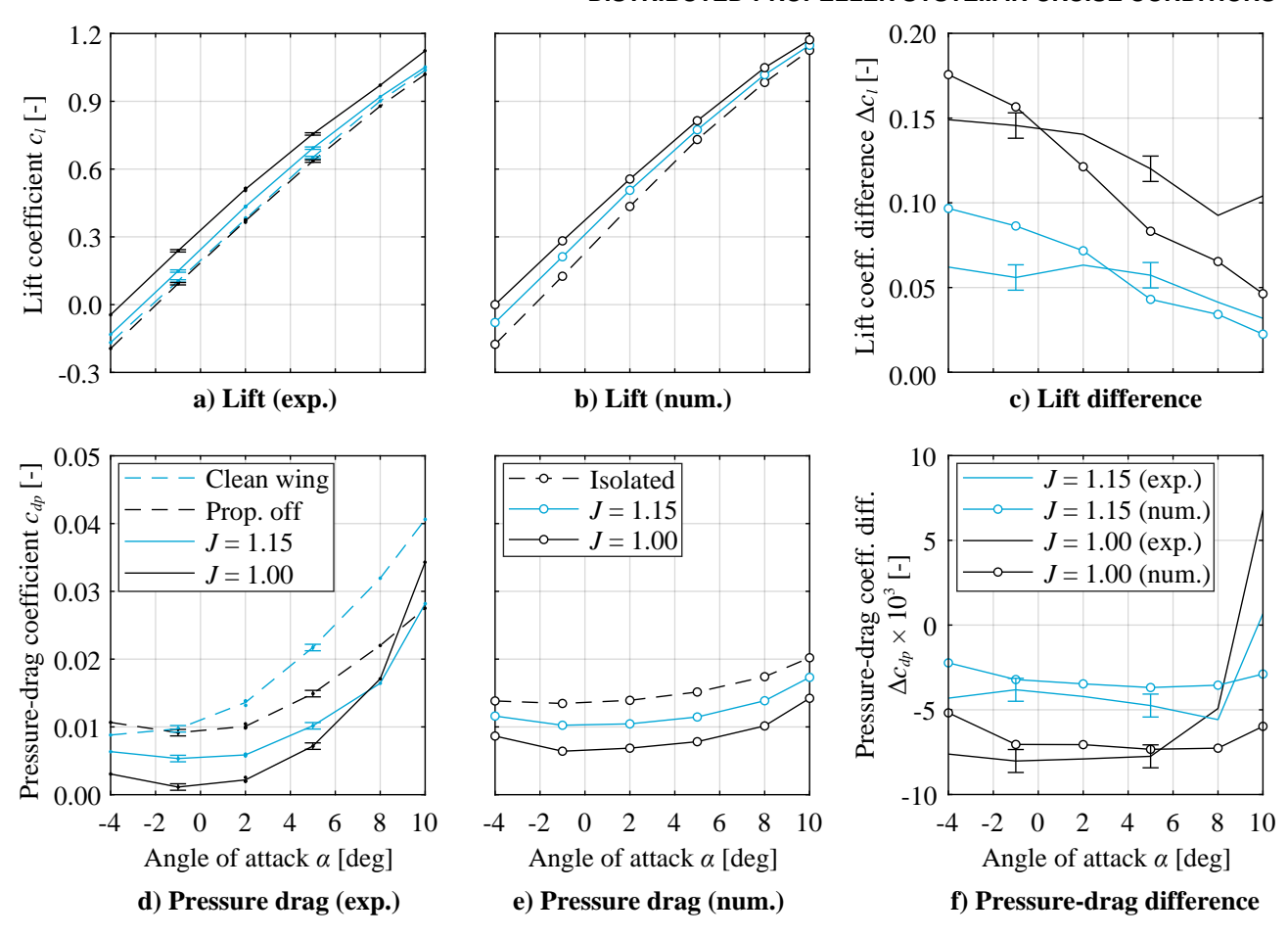


Figure 13 – Comparison of sectional lift and pressure-drag polars at $(y-y_p)/R = -0.7$.

the propeller creates an increase in axial velocity (i.e. lower static pressure) ahead of the propeller, and a decrease in axial velocity (i.e. higher static pressure) behind the propeller, as indicated by effect B in Fig. 4b. The impact of this effect on drag is highly dependent on the axial position, with the largest drag reductions occurring for propellers near the point of maximum thickness (see Refs. [15, 7]), since in that case the low and high pressure areas in front and behind the propeller affect forward- and backward-facing surfaces of the airfoil, respectively. However, at higher angles of attack, the drag reduction is decreased, and the interaction eventually leads to a drag increase with respect to the propeller-off case. This is especially evident at the high thrust setting (J=1.00, $T_{\rm c}\approx 0.41$), where the drag exceeds the propeller-off case above $\alpha=8^{\circ}$ due to the propeller-induced trailing-edge separation observed in Fig. 11d. At these high angles of attack, the numerical model provides significantly lower drag values than those obtained in the experiment (Fig. 13e). This is a consequence of the increased suction peak and delayed flow separation predicted by the numerical model. This confirms that the applicability of the numerical is limited to low or moderate angles of attack and thrust settings, that is, to cruise conditions.

These changes in wing performance are shown in Figs. 13c and 13f. A comparison of the lift "deltas" shows that the numerical model predicts the lift enhancement reasonably well for $J=1.15,~\alpha>2^{\circ}$. At lower angles of attack, the lift increase is over-estimated, as seen in Fig. 13c. This may be a result of the straight slipstream-tube approximation, although additional investigations would be required to confirm this. In any case, the corresponding c_l are lower than the ones that would typically be encountered throughout a flight profile $(c_l<0.4)$. At a higher thrust setting $(J=1.00,~T_c\approx0.4)$, the numerical model under-estimates the lift enhancement for $\alpha>0^{\circ}$. This is a consequence of the aforementioned challenges with respect to predicting the boundary-layer evolution under strong adverse pressure gradients. Therefore, in these conditions, which are more representative of a climb phase, the model is less accurate, and provides conservative results in terms of lift. Regarding the changes in pressure drag, Fig. 13f shows that the model under-estimates the drag reduction due to

OTWDP for low to moderate angles of attack, in both low and high thrust settings. At high angles of attack, the model over-estimates the drag reduction, because the trailing-edge flow separation that occurs in the experiment is not present to the same extent in the simulations.

Finally, to illustrate the beneficial effects of the OTW propellers on the wing performance, Fig. 14 provides the wing lift-to-drag ratio as a function of the lift coefficient, as obtained from the experiment. Since the forces correspond to the complete wing, the wing reference area $S_{\rm ref} = b \cdot c$ is used for normalization, though only 50% of the wing span is covered by the three propellers. Therefore, the average changes in lift-to-drag ratio for a full-span OTWDP system would be roughly double. The results are not compared to predictions of the numerical method, since the root junction flow and tip effects would not be captured by the model. For this plot, polynomial fits were applied to the lift and drag data, to allow an approximate comparison of the different cases at a constant lift coefficient. The graph includes a single data point at a very high thrust setting (J = 0.8, $T_{\rm c} \approx 1.0$), and present all results with the propeller installation located in its default mid-span position.

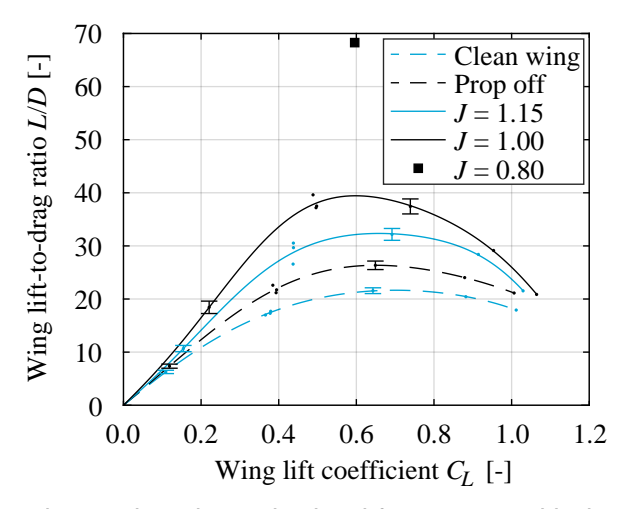


Figure 14 – Wing lift-to-drag ratio values obtained from external balance measurements. Dots indicate individual measurements ($S_{\text{ref}} = b \cdot c$).

As expected from the sectional drag polars, the lift-to-drag ratio of the propeller-off configuration is higher than the one of the clean wing. However, these balance measurements do not include the forces on the support sting and nacelles. Since the support sting and nacelle geometries are not representative of a practical application, the effect of the propellers themselves should be assessed by comparing the propeller-on to the propeller-off measurements, rather than to the clean-wing measurements. The increase in lift-to-drag ratio due to the OTW propellers is highest near the lift coefficient corresponding to maximum L/D. At a typical cruise lift coefficient of $C_L = 0.6$, the lift-to-drag ratio of the wing is increased by approximately 23% at a low thrust setting (J = 1.15, $T_c \approx 0.2$), and by 51% at a high thrust setting (J = 1.00, $T_c \approx 0.45$). This increase in L/D does not include the contribution of the propeller normal force to lift (see previous section), which would further increase the lift-to-drag ratio. As the thrust setting is further increased (J = 0.8), the drag approaches zero and the lift-to-drag ratio increases exponentially. This effect is comparable to the lip-thrust generated on ducts at high thrust settings (see e.g. Ref. [21]). It is important to highlight that these values are inherent to this specific experimental setup. For example, a change in the span-fraction covered by the OTW propellers would directly affect the overall lift-to-drag ratio. Moreover, the OTWDP system used in the experiment had a diameter-to-chord ratio of $D_P/c = 0.6$. Lower D_P/c values may be encountered in practice due to other constraints in the design process.

4.3 Limitations of the Numerical Method

Based on the comparisons performed so far, it appears that the numerical model provides acceptable but conservative results in terms of lift enhancement, pressure-drag reduction, and propeller normal-force increase, for typical cruise conditions ($T_c < 0.2$, $c_l \sim 0.5$). In these conditions, the predicted Δc_l and Δc_d values differ from the experimental data by approximately ± 0.02 and ± 0.001 , respectively. Note that, for the friction drag, no data is available for a direct comparison. However, since the

propeller leads to only small changes in the sectional pressure distribution in cruise conditions (see Fig. 11), XFOIL is assumed to predict the friction drag of the effective propeller-on airfoil with the same accuracy and limitations as it would do for a normal airfoil. Thus, no significant errors are expected in terms of friction drag as long as the flow remains attached over the entire airfoil. Moreover, the trends of the changes in lift, drag, and sectional pressure distributions also match the experiment and are in line with the observations of earlier studies [17, 15, 16]. The validation also shows that the model does not produce accurate results if flow separation occurs beneath the propellers.

These conclusions can be extrapolated to other geometries and operating conditions, with several limitations. Firstly, the operating conditions must be such that the flow remains attached. This imposes a limitation especially on the angle of attack and thrust-coefficient range, although the exact limit of attached flow depends on numerous factors. Given that the sensitivity of the boundary layer to the adverse pressure gradients induced by the propeller reduces with increasing Reynolds number, the model can be used at higher Reynolds numbers, but should not be used at lower Reynolds numbers than the ones used for the validation study ($Re_c = 6 \cdot 10^5$). Higher subsonic Mach numbers can also be evaluated, though the compressibility correction loses accuracy as the transonic regime is approached. Moreover, the propeller model is not sensitive to changes in the Reynolds number or Mach number, and is therefore likely to provide unreliable results in those conditions. Regarding the geometry of the system, the model is expected to be able to predict the interaction for a wide range of $D_{\rm P}/c$ values, since the velocities induced by the propeller on the wing and vice versa are predominantly caused by inviscid effects. The model is not accurate for cases where the size of the propeller is of the same order as the thickness of the wing boundary layer $(D_P/c \ll 1)$. Furthermore, due to the violation of the assumption of irrotational flow at the slipstream edge, the accuracy of the solution cannot be guaranteed for lower tip clearances than the one used in the validation study. Thus, the combination of incidence angle, axial position, and tip clearance, should be such that the slipstream maintains a separation from the wing surface of at least $\varepsilon/R > 0.05$. Finally, the axial position of the propeller should not be close to the leading edge ($x_P > 0.2$), since the leading edge is not modified in the inverse-design process. Nevertheless, the validation study shows that, within these bounds, the method is capable of estimating the changes in wing and propeller performance with an accuracy that is appropriate of low-order methods for conceptual design purposes. Therefore, it is used in the following section to analyze the performance of the wing and propeller for different operating conditions.

5. Effect of Operating Conditions

Now that the capabilities and limitations of the numerical model have been identified, the model is used in this section to understand how the performance of an OTWDP system varies with different operating conditions. To make the comparisons more representative of a full-scale application, the freestream Reynolds number and Mach number are set to $Re_c = 10^7$ and M = 0.4, respectively. This affects the wing performance but, as discussed in Sec. 3.1 the propeller performance estimates are not sensitive to Re or M for a given inflow condition. Additionally, a blade pitch of 45° is used as baseline, since this setting provides maximum efficiency at a typical cruise thrust setting. An overview of the operating conditions selected as baseline for the following analyses is provided in Table 2. Moreover, to make the results representative of a distributed-propulsion system with many propellers, the number of propellers modeled is increased to 7. This value was selected based on a separate sensitivity study, which showed that for $N_P = 7$ the changes in wing performance beneath the middle propeller were comparable to a configuration with $N_P \to \infty$. The baseline values of all other geometrical parameters are maintained identical to those of the experimental/validation study $(D_P/c = 0.6, x_P/c = 0.8, i_P = 10.2^\circ)$, including the fixed boundary-layer transition location.

Furthermore, for a fair comparison, the analyses of the following sections are performed at constant net vertical and axial forces, unless explicitly mentioned otherwise. Vertical and axial force coefficients of $C_{L,\rm net} = (L+F_{z,\rm P})/(q_{\infty}S_{\rm ref}) = 0.5$ and $C_{D,\rm net} = (D+F_{x,\rm P})/(q_{\infty}S_{\rm ref}) = -0.051$ are used, respectively, where the reference area $S_{\rm ref}$ corresponds to the wing segment of span $D_{\rm P}+d$ covered by the middle propeller. These values are considered representative of cruise conditions and are based on back-of-the-envelope calculations using reference data of an ATR 72-600 [41] ($C_L \approx 0.5$, $T_c \approx 0.1$). For each data point, the angle of attack and advance ratio of the OTW system are adjusted to produce

these values. The effect of different lift and thrust settings is described in the following subsections, along with the effect of Reynolds number on the changes in wing performance. However, first the effect of the propellers' blade pitch setting is addressed, to illustrate how the changes in propeller efficiency are computed in subsequent sections.

Table 2 – Baseline operating conditions used in the parameter sweeps.

Parameter	Value
Blade pitch $\beta_{0.7R}$ [deg]	45
Reynolds number Re_c [-]	10^{7}
Mach number M [-]	0.4
Net vertical force coefficient $C_{L,\text{net}}$ [-]	0.5
Net axial force coefficient $C_{D,\mathrm{net}}$ [-]	-0.051

5.1 Blade Pitch Setting

Figure 15 presents the axial force, torque, and efficiency of the propeller for two blade pitch angles, for the isolated and installed configurations. For simplicity, these curves are produced by varying the advance ratio while maintaining the angle of attack of the wing constant; i.e., the net forces of the system are not maintained. The figure shows that, for this propeller position, its thrust, torque, and efficiency are reduced in installed conditions, as expected from Fig. 10. The point A shown on the isolated-propeller performance curves corresponds to the advance ratio at which maximum propeller efficiency is obtained. As shown in Fig. 15c, when installing the propeller over the wing while

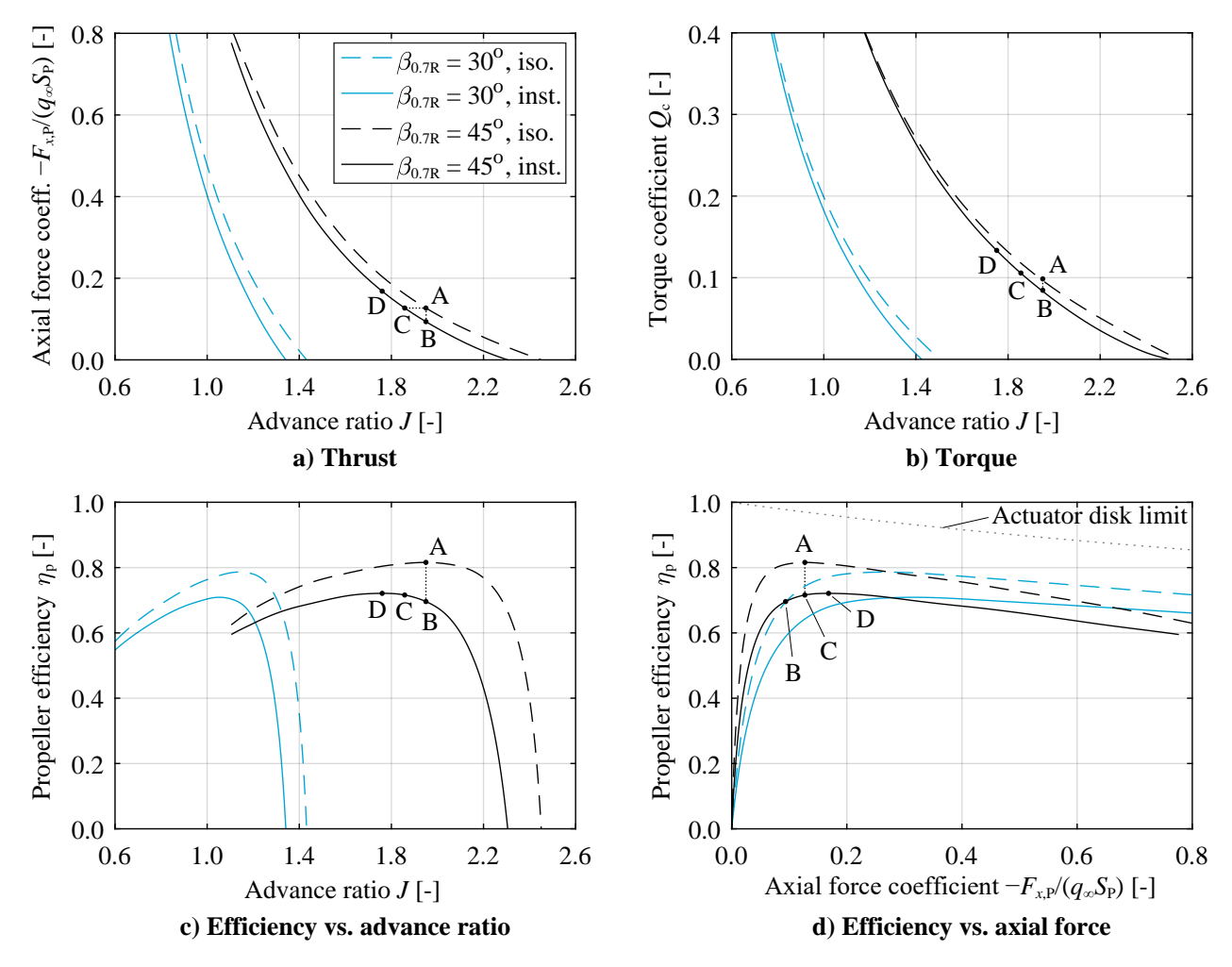


Figure 15 – Comparison of propeller performance parameters in isolated and installed conditions, obtained numerically for two different blade pitch settings.

maintaining a constant advance ratio, the propeller efficiency drops from point A to point B. However, this is not a fair comparison. Instead, for a fixed blade pitch, a comparison at constant thrust is more representative. In this case, the propeller-efficiency penalty $(A\rightarrow C)$ would be less than in the case of an installation at constant advance ratio $(A\rightarrow B)$. For this specific set of operating conditions, $\eta_{p,B}$ and $\eta_{p,C}$ only differ by 2%; however, in other OTW scenarios, the difference between comparisons at constant thrust and constant advance ratio can be substantially larger [15].

The propeller-efficiency penalty is further reduced if a variable-pitch propeller is considered. In that case, the reduction in propeller efficiency from point A to point D is more representative, since the blade pitch would be adjusted to always operate at the maximum efficiency for a given thrust setting. Although point D does not correspond to the same thrust setting as point A, a slight adjustment in the blade pitch to ensure equal thrust would lead to comparable propeller-efficiency values. In fact, in first approximation, a small change in blade pitch translates the performance curves horizontally along the *J*-axis. While Fig. 15c shows that the maximum efficiency is slightly lower for $\beta_{0.7R} = 30^{\circ}$ than for $eta_{0.7R} = 45^{
m o}$, the ratio of the maxima $\eta_{
m p,max,inst}/\eta_{
m p,max,iso} = \eta_{
m p,D}/\eta_{
m p,A}$ is practically constant, especially for small changes in blade pitch around a nominal condition [29]. This implies that, for a variable-pitch propeller, the ratio $\eta_{p,max,inst}/\eta_{p,max,iso}$ can be computed for a given blade-pitch setting, and applied to different thrust settings, assuming that the propeller always operates at the optimum pitch angle. For this reason, in the following sections, the isolated and installed configurations are evaluated at a constant net axial force (i.e., at approximately the same thrust) to compute the change in lift-to-drag ratio, but the change in propeller efficiency $\eta_{\rm p,inst}/\eta_{\rm p,iso}$ is calculated as the ratio of the maximum efficiencies obtained for a determined pitch setting and inflow conditions, $\eta_{p,max,inst}/\eta_{p,max,iso}$. This avoids misleading conclusions regarding changes in propeller efficiency due to operation at a suboptimal advance ratio. This also does not affect the changes in wing performance, since they depend on the thrust coefficient T_c , and not on how efficiently the thrust is generated (see Sec. 3.2).

5.2 Lift Coefficient

Figure 16a shows how the lift-to-drag ratio of the wing segment beneath a propeller varies with net vertical force at a constant net axial force. The net vertical force can be interpreted as the effective system lift coefficient, $C_{L,\text{net}}$. The difference between isolated and installed conditions improves with increasing $C_{L,\text{net}}$. The L/D increase at given net vertical force, for example $\Delta(L/D)_1$ at $C_{L,\text{net}}=0.8$, is smaller than the L/D benefit obtained at a given angle of attack (e.g. $\Delta(L/D)_2$ at $\alpha=3.2^{\circ}$). In other words, the improvement in installed lift-to-drag ratio as the net vertical force increases is partially due to the increase in angle-of-attack, which moves the airfoil closer to its optimum L/D. This is the case for this particular airfoil and range of operating conditions; however, if a complete wing were

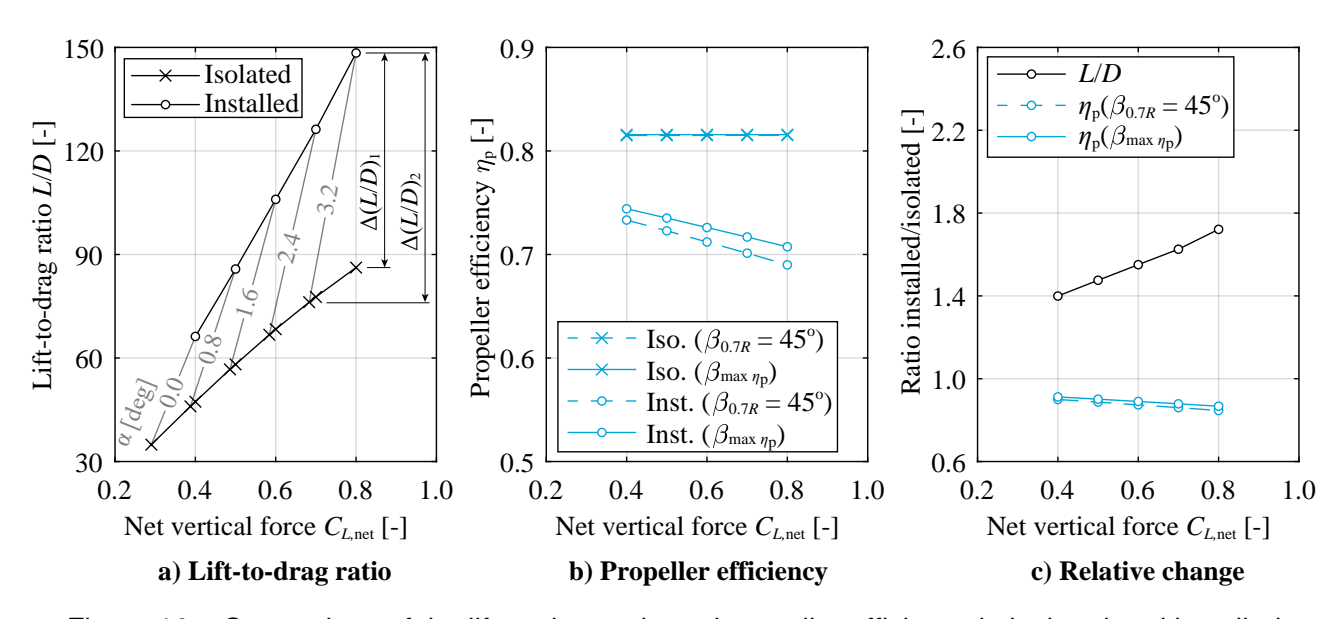


Figure 16 – Comparison of the lift-to-drag ratio and propeller efficiency in isolated and installed conditions, for a fixed net axial force ($C_{D,\text{net}} = -0.051$) and varying vertical force. Numerical results.

considered, it would likely be designed to present a maximum L/D in this range of lift coefficients (see e.g. Fig. 14). Around that maximum, the isolated-wing L/D would be approximately constant, and therefore $\Delta(L/D)_2$ is more representative of the potential lift-to-drag-ratio benefit of OTWDP than $\Delta(L/D)_1$. This is analogous to the effect of blade pitch discussed in the previous section: for a fair comparison of the performance "deltas", the (blade) airfoil should be near the optimum angle of attack in both the isolated and installed conditions.

Regarding the propeller performance, Fig. 16b shows how the installed propeller efficiency decreases with increasing net vertical force, due to a more pronounced velocity gradient above the airfoil and a lower contribution of the thrust and normal-force vectors to the net propeller force in the direction of flight. The propeller-efficiency penalty is reduced if the propeller pitch is adapted to operate near maximum efficiency instead of keeping it constant at $\beta_{0.7R} = 45^{\circ}$, as discussed in Sec. 5.1 When comparing the ratio between installed and isolated performance (Fig. 16c), the lift-to-drag ratio is found to increase by 40% to 70% in this range of lift coefficients, while the propeller efficiency is decreased by 10% to 15%.

5.3 Thrust Setting

To demonstrate the effect of thrust setting, Fig. 17a shows how the lift-to-drag ratio varies with net axial force. The isolated-wing L/D is constant, since it is independent of propeller thrust. When the axial force produced by the propeller equals the drag of the wing segment ($C_{D,\text{net}} = 0$), the L/D difference between isolated and installed conditions is negligible, since the thrust setting is low. An increased thrust setting (i.e. a more negative $C_{D,\text{net}}$) leads to an increase in L/D, as already evidenced in the experimental data in Fig.14. For very high thrust settings, L/D tends to infinity as the drag of the wing segment approaches zero due to the propeller-induced suction near the leading edge. Note that the drag of the wing segment may eventually become negative; in other words, the wing segment can produce thrust at very high propeller thrust coefficients—for example at the start of take-off.

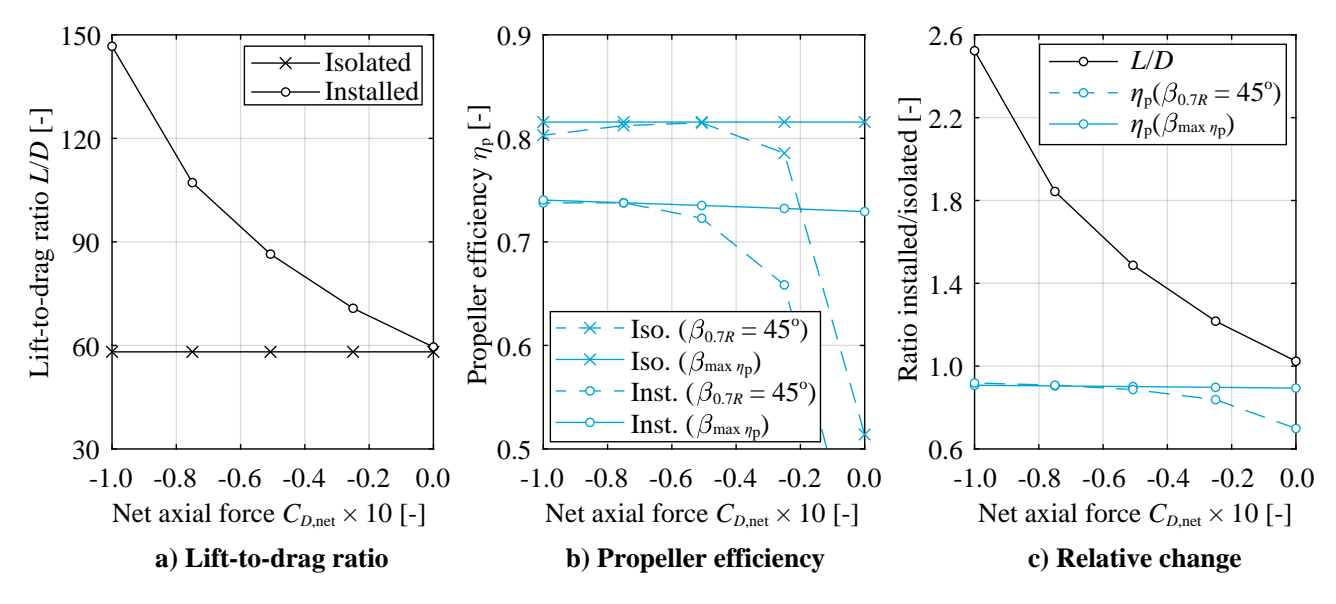


Figure 17 – Comparison of the lift-to-drag ratio and propeller efficiency in isolated and installed conditions, for a fixed net vertical force ($C_{L,net} = 0.5$) and varying axial force. Numerical results.

The propeller efficiency presented in Fig. 17b shows very different trends between the cases at constant and variable pitch angle. For a fixed pitch angle, the curves follow the shape of the $\eta_{\rm p}(J)$ curve (see Fig. 15), since more negative $C_{D,\rm net}$ values correspond to lower advance ratios. If the blade pitch is adapted to maximize $\eta_{\rm p}$ in each condition, however, the variations with $C_{D,\rm net}$ are much smaller. In that case, the installed propeller efficiency improves slightly with more negative $C_{D,\rm net}$ values. This occurs because, at a higher thrust setting, a lower angle-of-attack is required to maintain the same net vertical force, and therefore the velocity gradient at the propeller location is reduced. Hence, the overall installed system performance—and particularly the lift-to-drag ratio—is improved at higher thrust settings, as reflected in Fig. 17c.

5.4 Reynolds Number

This section describes how the wing lift-to-drag ratio is affected by the Reynolds number, for a constant net axial force, net vertical force, and transition location. The propeller efficiency is not discussed, since the propeller-performance model is not sensitive to the Reynolds number. However, since the effect of the propeller on the wing depends primarily on the thrust coefficient, the changes in L/D due to changes in propeller performance when varying Re_c are negligible. The resulting L/D curves are shown in Fig. 18 for two Mach numbers: one comparable to the wind-tunnel conditions (M=0.1), and one representative of a turboprop cruise condition (M=0.4). The isolated-wing curves show how the lift-to-drag ratio of the wing segment increases almost linearly with the logarithm of the Reynolds number. Note that, if the wing surface presented no disturbances and no transition location were enforced, the slope of the L/D curve would be lower since the extent of turbulent flow on the airfoil would increase as the transition location moves forward with increasing Re_c . In order to maintain a constant $C_{L,\rm net}=0.5$, the angle of attack of the airfoil decreases with both increasing Reynolds number and Mach number. Due to the minor reduction in angle of attack, the lift-to-drag ratio of the wing segment is also slightly lower for M=0.4 than for M=0.1 (see Fig. 16a).

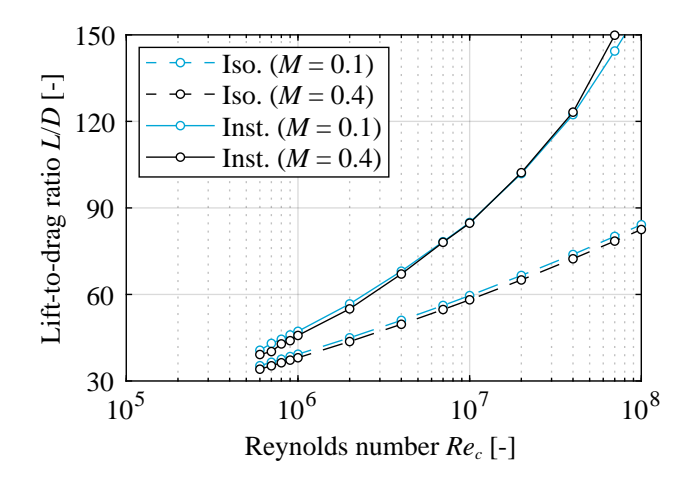


Figure 18 – Effect of the wing-chord-based Reynolds number and freestream Mach number on the lift-to-drag ratio of the wing segment in isolated and installed conditions, for a constant net axial force $(C_{D,\text{net}}=-0.051)$, net vertical force $(C_{L,\text{net}}=0.5)$, and transition location $(x_{\text{tr,ss}}/c=0.05, x_{\text{tr,ps}}/c=0.10)$.

In the installed case, the lift-to-drag ratio increases more rapidly with Reynolds number than in the isolated case. This is a result of the pressure-drag reduction due to the OTW propellers, which decreases the denominator of "L/D", and therefore a given change in profile drag due to a variation in Reynolds number has a relatively larger impact on the lift-to-drag ratio. Moreover, Fig. 18 shows that the installed case at M=0.4 presents a slightly steeper slope than at M=0.1. This occurs because the changes in C_p due to compressibility effects are more significant for larger $|C_p|$ values $(C_p \approx C_{p,M=0}/\sqrt{1-M^2})$, and the largest changes in pressure coefficient due to the propeller occur near the leading edge (see Fig. 11c). Therefore, at higher (subsonic) Mach numbers, the leading-edge suction induced by the propellers is enhanced, leading to a minor reduction in pressure drag compared to the result at lower Mach number. This effect is more pronounced at higher Reynolds numbers, where the contribution of the propeller-induced lift to total wing lift was found to be slightly higher. In any case, the differences between M=0.1 and M=0.4 are small in the installed case, and comparable to the noise in the curves due to discretization and convergence errors. Overall, Fig. 18 reaffirms that compressibility effects play only a minor role for the range of Mach numbers evaluated here.

5.5 Implications for Aircraft Performance

The ratios between installed and isolated conditions in Figs. 16–18 suggest a substantial increase in aero-propulsive efficiency, $\eta_p(L/D)$, for most operating conditions. However, it should be emphasized that the lift-to-drag ratio benefit applies to only (part of) the wing, but other parts of the aircraft also contribute to lift or drag. Likewise, if the distributed-propulsion aircraft presents both OTW pro-

pellers and propellers placed at a different location, then the propeller-efficiency penalty of the OTW propellers has less impact on the average propeller efficiency. Therefore, the overall increase or decrease in aircraft-level $\eta_p(L/D)$ will depend on the aircraft configuration.

Moreover, the analyses shown here have been performed for a determined geometry. However, previous studies have already demonstrated a strong sensitivity to parameters such as the axial propeller position [15, 9, 29] and diameter-to-chord ratio [16]. Recent exploratory investigations using the method presented here also indicate a strong influence of the propeller incidence angle relative to the wing [39]. For different designs, the impact on lift-to-drag ratio and propeller efficiency can vary significantly. For example, a propeller placed close to the trailing edge may in fact present an increase in propeller efficiency, due the flow deceleration near the trailing-edge stagnation point and an angle-of-attack effect on the propeller [39, 29]. In that case, the lift-to-drag ratio is comparable to the uninstalled case, or worse. Hence, the optimum design again depends on how the $\Delta(L/D)$ of the OTWDP wing segment relates to the overall aircraft L/D, and how the $\Delta\eta_{\rm p}$ of the OTW propellers relate to the overall aircraft geometries should be investigated in future work, including the effect of the nacelles and support pylons.

6. Conclusions & Recommendations

This study combines experimental and numerical analyses to determine the aero-propulsive performance of a simplified over-the-wing distributed-propulsion (OTWDP) system for various operating conditions. A wind-tunnel experiment featuring a rectangular wing with three over-the-wing (OTW) propellers of diameter-to-chord ratio $D_{\rm P}/c=0.6$ placed at 80% chord, without duct, is performed to explore the potential performance benefits and to serve as validation data for the numerical method. The simplified numerical method combines 2D panel methods, a slipstream-vortex model, and a propeller performance model to calculate the impact of the propellers on the wing and vice-versa. The numerical method is found to predict the changes system performance with sufficient accuracy for conceptual design-space exploration purposes, for wing and propeller loading conditions representative of a cruise condition. The match with experimental data confirms that, in such conditions, the effect of an OTW propeller on the sectional wing pressure distribution can be modeled as an equivalent increase in angle of attack combined with a change in upper-surface camber. However, the model is not accurate if flow separation occurs beneath the propeller (i.e. at high lift or thrust coefficients), and in its current implementation, the changes in propeller performance are not sensitive to Revnolds number or Mach number.

Results from the experiment, where roughly half of the wing span is covered by the three propellers, show that the propellers increase the lift-to-drag ratio of the rectangular wing by 23% and 51% at low ($T_{\rm c}\approx 0.2$) and high ($T_{\rm c}\approx 0.45$) thrust settings, respectively. This does not account for forces on the nacelles or support sting. The numerical calculations present the same trends, estimating a 40% to 70% increase in sectional lift-to-drag ratio beneath the propellers for typical cruise lift coefficient, thrust coefficient, and Reynolds number. However, the propeller efficiency is found to decrease by 10% to 15%. An assessment of different operating conditions illustrates that, for a fair comparison of installed versus uninstalled performance, it is vital to design the system such that the wing and propeller operate near the optimum angle of attack and blade-pitch setting, respectively, at the desired cruise lift and thrust setting. Not doing so may lead to a significant under-estimation of the aero-propulsive performance benefits due to propeller—wing interaction. Moreover, the parameter sweeps show that both the wing and propeller performance improve with increasing lift and thrust coefficients, indicating that the OTWDP system can present a particularly good climb performance.

The findings of this study demonstrate significant aero-propulsive performance benefits at subsystem (i.e. propeller plus wing segment) level. However, additional investigations are required to determine whether the factor $\eta_{\rm p}(L/D)$ is also increased when the rest of the aircraft and a more realistic geometry are considered. Regarding the geometry, the impact of axial propeller position, propeller incidence angle, and diameter-to-chord ratio should be studied carefully, as previous research has shown a large sensitivity to these design parameters. Moreover, if a duct is required to improve the propeller efficiency or the acoustic signature of the system, it will affect the changes in performance due to aerodynamic interaction, as well as the optimal propeller position. Thus, the influence of not

only the nacelles but also a potential duct should be investigated in more detail. Future research focusing on these topics will enhance the understanding of OTWDP system performance and allow new forms of propulsion-system integration that can improve the efficiency of novel (hybrid-)electric aircraft configurations.

7. Contact Author Email Address

Corresponding author: R.deVries@tudelft.nl

8. Copyright Statement

The authors confirm that they, and/or their company or organization, hold copyright on all of the original material included in this paper. The authors also confirm that they have obtained permission, from the copyright holder of any third party material included in this paper, to publish it as part of their paper. The authors confirm that they give permission, or have obtained permission from the copyright holder of this paper, for the publication and distribution of this paper as part of the ICAS proceedings or as individual off-prints from the proceedings.

Acknowledgments

This research is funded by the European Union's Horizon 2020 Clean Sky 2 Large Passenger Aircraft program (CS2-LPA-GAM-2020/2021-01), under grant agreement No. 945583. The authors would like to thank Nando van Arnhem for providing the propeller performance model and for his assistance during the preparation of the wind-tunnel test. The help of Pedro López Pernas, Leandro Rêgo, and the DNW staff members during the test campaign is also gratefully acknowledged. The authors would also like to thank Peter den Dulk, Steve van Herk, Frank Schilders, Ed Roessen, Leon Roessen, and Rob van der List from the DEMO division for the manufacturing of the wind-tunnel model, and Roelof Vos for his guidance and feedback during the writing process.

References

- [1] Advisory Council for Aviation Research and Innovation in Europe (ACARE). Strategic research & innovation agenda, 2017 update, Vol. 1. Advisory Council for Aviation Research and Innovation in Europe, 2017.
- [2] J. E. Green. Air Travel-Greener by Design. Mitigating the environmental impact of aviation: opportunities and priorities. *The Aeronautical Journal*, 109(1099):361–418, 2005.
- [3] National Academies of Sciences, Engineering, and Medicine. *Commercial Aircraft Propulsion and Energy Systems Research: Reducing Global Carbon Emissions*. National Academies Press, 2016.
- [4] B. J. Brelje and J. R. R. A. Martins. Electric, hybrid, and turboelectric fixed-wing aircraft: A review of concepts, models, and design approaches. *Progress in Aerospace Sciences*, 104:1–19, 2019.
- [5] S. Sahoo, X. Zhao, and K. Kyprianidis. A review of concepts, benefits, and challenges for future electrical propulsion-based aircraft. *Aerospace*, 7(44), 2020.
- [6] R. de Vries, M. F. M. Hoogreef, and R. Vos. Aeropropulsive efficiency requirements for turboelectric transport aircraft. AIAA Scitech 2020 Forum, Orlando, FL, USA, January 6-10 2020.
- [7] J. L. Johnson Jr. and E. R. White. Exploratory Low-Speed Wind-Tunnel Investigation of Advanced Commuter Configurations Including an Over-the-Wing Propeller. AIAA Aircraft Design, Systems and Technology Meeting, Fort Worth, TX, USA, October 17-19 1983.
- [8] L. Müller, W. Heinze, D. Kožulović, M. Hepperle, and R. Radespiel. Aerodynamic Installation Effects of an Over-the-Wing Propeller on a High-Lift Configuration. *Journal of Aircraft*, 51(1):249–258, 2014.
- [9] L. Müller, D. Kožulović, M. Hepperle, and R. Radespiel. The influence of the propeller position on the aerodynamics of a channel wing. Deutscher Luft-und Raumfahrt Kongress, Berlin, Germany, September 2012.
- [10] S. A. Bölk, R. de Vries, N. van Arnhem, and L. L. M. Veldhuis. Numerical investigation of propeller–flap interaction in inclined over-the-wing distributed-propulsion systems. AIAA Scitech 2021 Forum, Virtual Event, January 11-15 & 19-21 2021.
- [11] R. de Vries, N. van Arnhem, F. Avallone, D. Ragni, R. Vos, G. Eitelberg, and L. L. M. Veldhuis. Experimental investigation of over-the-wing propeller-boundary-layer interaction. *AIAA Journal*, 59(6):2169–2182, 2021.

- [12] W. C. Sleeman Jr. and W. C. Hohlweg. Low-speed wind-tunnel investigation of a four-engine upper surface blown model having a swept wing and rectangular and D-shaped exhaust nozzles. NASA Technical Note D-8061, 1975.
- [13] J. Delfs, B. Faßman, N. Lippitz, M. Lummer, M. Mößner, L. Müller, K. Rurkowska, and S. Uphoff. SFB 880: aeroacoustic research for low noise take-off and landing. *CEAS Aeronautical Journal*, 5(4):403–417, 2014.
- [14] C. Dornier. The dornier do.x. seaplane: Full technical details of the design and construction of the largest flying boat yet built. *Aircraft Engineering and Aerospace Technology*, 1(10):339–341, 1929.
- [15] L. L. M. Veldhuis. Propeller wing aerodynamic interference. PhD Dissertation, Delft University of Technology, 2005.
- [16] E. A. P. Marcus, R. de Vries, A. Raju Kulkarni, and L. L. M. Veldhuis. Aerodynamic investigation of an over-the-wing propeller for distributed propulsion. 2018 AIAA Aerospace Sciences Meeting, Kissimmee, FL, USA, January 8-12 2018.
- [17] R. K. Cooper, W. J. McCann, and A. Q. Chapleo. Over wing propeller aerodynamics. *ICAS Proceedings* (AIAA), 18:266–273, 1992.
- [18] J. Hermetz, M. Ridel, and C. Döll. Distributed electric propulsion for small business aircraft: A conceptplane for key-technologies investigations. 30th ICAS Congress, Daejeon, South Korea, 2016.
- [19] A. T. Wick, J. R. Hooker, C. J. Hardin, and C. H. Zeune. Integrated aerodynamic benefits of distributed propulsion. 53rd AIAA Aerospace Sciences Meeting, Kissimmee, FL, USA, January 5-9 2015.
- [20] A. T. Perry, T. Bretl, and P. J. Ansell. Aeropropulsive coupling effects on a general-aviation aircraft with distributed electric propulsion. *Journal of Aircraft*, 2021.
- [21] H. F. M. Bento, R. de Vries, and L. L. M. Veldhuis. Aerodynamic performance and interaction effects of circular and square ducted propellers. AIAA Scitech 2020 Forum, Orlando, FL, USA, January 6-10 2020.
- [22] L. M. M. Boermans and P. B. Rutten. Two-dimensional Aerodynamic Characteristics of Airfoil NLF-MOD22 with Fowler Flap. TU Delft Internal Report LSW-95-3, 1995.
- [23] S. Biser, M. Filipenko, M. Boll, N. Kastner, G. Atanasov, M. Hepperle, D. Keller, D. Vechtel, and M. Noe. Design space exploration study and optimization of a distributed turbo-electric propulsion system for a regional passenger aircraft. AIAA Propulsion and Energy Forum (virtual event), August 24-28 2020.
- [24] M. D. Patterson. Conceptual design of high-lift propeller systems for small electric aircraft. PhD Dissertation, Georgia Institute of Technology, 2016.
- [25] A. T. Perry, P. J. Ansell, and M. F. Kerho. Aero-propulsive and propulsor cross-coupling effects on a distributed propulsion system. *Journal of Aircraft*, 55(6):2414–2426, 2018.
- [26] N. van Arnhem, R. de Vries, T. Sinnige, R. Vos, G. Eitelberg, and L. L. M. Veldhuis. Engineering method to estimate the blade loading of propellers in nonuniform flow. *AIAA Journal*, 58(12):5332–5346, 2020.
- [27] R. de Vries, N. van Arnhem, T. Sinnige, R. Vos, and L. L. M. Veldhuis. Aerodynamic interaction between propellers of a distributed-propulsion system in forward flight. *Aerospace Science and Technology*, 118, 2021.
- [28] J. Katz and A. Plotkin. Low-speed aerodynamics. Cambridge University Press, 13th edition, 2001.
- [29] A. van Arnhem. Unconventional propeller–airframe integration for transport aircraft configurations. PhD Dissertation, Delft University of Technology, 2022.
- [30] M. P. Metcalfe. On the modelling of a fully-relaxed propeller slipstream. AIAA/SAE/ASME/ASEE 21th Joint Propulsion Conference, Monterey, CA, USA, July 8-10 1985.
- [31] L. R. Miranda and J. E. Brennan. Aerodynamic effects of wingtip-mounted propellers and turbines. 4th Applied Aerodynamics Conference, San Diego, CA, USA, June 9-11 1986.
- [32] J. B. de Vaal, M. O. L. Hansen, and T. Moan. Validation of a vortex ring wake model suited for aeroelastic simulations of floating wind turbines. *Journal of Physics: Conference Series*, 555, 012025, 2014.
- [33] S. S. Yoon and S. D. Heister. Analytical formulas for the velocity field induced by an infinitely thin vortex ring. *International Journal for Numerical Methods in Fluids*, 44:665–672, 2004.
- [34] M. Drela. XFOIL: An Analysis and Design System for Low Reynolds Number Airfoils. In: Mueller T.J. (eds) Low Reynolds Number Aerodynamics. Lecture Notes in Engineering, Vol. 54, Springer, Berlin, Germany, 1989.

- [35] J. D. Anderson. Fundamentals of Aerodynamics. McGraw-Hill, 2nd edition, 1991.
- [36] M. Drela and H. Youngren. Xfoil 6.9 user primer, 2001. Accessed 26 August 2016.
- [37] M. J. Lighthill. A new method of two-dimensional aerodynamic design. Aeronautical Research Council, Reports and Memoranda, No. 2112, April 1945.
- [38] B. M. Kulfan. Universal parametric geometry representation method. *Journal of Aircraft*, 45(1):142–158, 2008.
- [39] R. de Vries. Hybrid-electric aircraft with over-the-wing distributed propulsion: Aerodynamic performance and conceptual design. PhD Dissertation, Delft University of Technology, 2022.
- [40] L. Müller, J. Friedrichs, and D. Kožulović. Unsteady flow simulations of an over-the-wing propeller configuration. 50th AIAA/ASME/SAE/ASEE Joint Propulsion Conference, Cleveland, OH, USA, July 28-30 2014.
- [41] M. Lambert and F. T. Jane. *Jane's All The World's Aircraft*. Jane's Information Group, eighty-first edition, 1990-91.